

1 **Proteomics of autophagy deficient macrophages reveals enhanced
2 antimicrobial immunity via the oxidative stress response**

3

4 Timurs Maculins^{1,6}, Erik Verschueren², Trent Hinkle², Patrick Chang³, Cecile
5 Chalouni³, Junghyun Lim¹, Anand Kumar Katakam³, Ryan C. Kunz⁷, Brian K.
6 Erickson⁷, Ting Huang⁸, Meena Choi⁸, Tsung-Heng Tsai^{8,9}, Olga Vitek⁸, Mike
7 Reichelt³, John Rohde⁴, Ivan Dikic^{5,6*}, Donald S. Kirkpatrick^{2*}, Aditya Murthy^{1*}.

8

9 **Affiliations**

10 ¹Department of Cancer Immunology, Genentech, South San Francisco, CA, USA.

11 ²Department of Microchemistry, Proteomics and Lipidomics, Genentech, South San
12 Francisco, CA, USA.

13 ³Department of Pathology, Genentech, South San Francisco, CA, USA.

14 ⁴Department of Microbiology and Immunology, Dalhousie University, Canada.

15 ⁵Department of Infectious Diseases, Genentech, South San Francisco, CA, USA.

16 ⁶Institute of Biochemistry II, Goethe University, Frankfurt am Main, Germany.

17 ⁷IQ Proteomics LLC, Cambridge, MA, USA.

18 ⁸Khoury College of Computer Sciences, Northeastern University, Boston, MA, USA.

19 ⁹Department of Mathematical Sciences, Kent State University, Kent, OH, USA.

20

21 *These authors jointly supervised this work.

22

23 **Correspondence**

24 Aditya Murthy: murthy.aditya@gene.com

25 Donald Kirkpatrick: kirkpatrick.donald@gene.com

26 Ivan Dikic: dikic@biochem2.uni-frankfurt.de

27

28

29 **Impact statement**

30 Maculins *et al* utilize multiplexed mass spectrometry to show that loss of the
31 autophagy gene *Atg16l1* in macrophages enhances antimicrobial immunity against
32 intracellular pathogens via the oxidative stress response.

33 **Abstract**

34 Defective autophagy is associated with chronic inflammation. Loss-of-function
35 of the core autophagy gene Atg16l1 increases risk for Crohn's disease by enhancing
36 innate immunity in macrophages. However, autophagy also mediates clearance of
37 intracellular pathogens. These divergent observations prompted a re-evaluation of
38 ATG16L1 in antimicrobial immunity. In this study, we found that loss of Atg16l1 in
39 macrophages enhanced the killing of virulent *Shigella flexneri* (*S.flexneri*), an enteric
40 bacterium that resides within the cytosol by escaping all membrane-bound
41 compartments. Quantitative multiplexed proteomics revealed that ATG16L1
42 deficiency significantly upregulated proteins involved in the glutathione-mediated
43 antioxidant response to compensate for elevated oxidative stress, which also
44 promoted *S.flexneri* killing. Consistently, myeloid cell-specific deletion of Atg16l1
45 accelerated bacterial clearance *in vivo*. Finally, pharmacological modulation of
46 oxidative stress by suppression of cysteine import conferred enhanced microbicidal
47 properties to wild type macrophages. These findings demonstrate that control of
48 oxidative stress by ATG16L1 regulates antimicrobial immunity against intracellular
49 pathogens.

50

51 **Introduction**

52 Effective immunity against enteric pathogens requires complex signaling to
53 coordinate the inflammatory response, pathogen clearance, tissue remodeling and
54 repair (Maloy and Powrie, 2011). Autophagy, a cellular catabolic pathway that
55 eliminates cytosolic cargo via lysosomal degradation, has emerged as an important
56 regulator of mucosal immunity and inflammatory bowel disease (IBD) etiology.
57 Genome-wide association studies linked a missense variant (T300A) in the core
58 autophagy gene *Atg16l1* with increased risk for inflammatory bowel diseases (Hampe
59 et al., 2007; Rioux et al., 2007). Later studies demonstrated that this variant
60 contributes to enhanced caspase-mediated degradation of the ATG16L1 protein
61 (Lassen et al., 2014; Murthy et al., 2014). Genetic loss-of-function of core autophagy
62 genes including *Atg16l1* increases secretion of pro-inflammatory cytokines by
63 macrophages in response to toll-like receptor (TLR) activation (Lim et al., 2019;
64 Saitoh et al., 2008). This contributes to increased mucosal inflammation, driving
65 resistance to extracellular pathogens such as *Citrobacter rodentium* (Marchiando et
66 al., 2013; Martin et al., 2018) and pathogenic *Escherichia coli* (Wang et al., 2019).

67 Defective autophagy in the myeloid compartment also confers enhanced
68 antimicrobial immunity against certain intracellular pathogens, such as *Salmonella*
69 *typhimurium* (*S.typhimurium*) and *Listeria monocytogenes* via induction of type I and
70 II interferon responses (Samie et al., 2018; Wang et al., 2020). Thus, autophagy acts
71 as an immuno-suppressive pathway in antimicrobial immunity *in vivo*.

72 Targeted elimination of intracellular pathogens by xenophagy, a form of
73 selective autophagy, is well-described in cellular model systems (Bauckman et al.,
74 2015). In contrast to non-selective autophagy triggered by nutrient stress, xenophagy
75 functions to eliminate intracellular bacteria by sequestering them in autophagosomes
76 and shuttling them to the degradative lysosomal compartment. Pathogenic bacteria
77 have evolved mechanisms to either evade capture by the autophagy machinery, as
78 by *S.typhimurium* and *Shigella flexneri* (*S.flexneri*) (Birmingham et al., 2006;
79 Campbell-Valois et al., 2015; Dong et al., 2012; Martin et al., 2018; Xu et al., 2019b)
80 or attenuate autophagic flux as by *Legionella pneumophila* (Choy et al., 2012).
81 *S.typhimurium* primarily resides in a protective compartment known as the
82 *Salmonella* containing vacuole (SCV). There it prevents formation of the ATG5-
83 ATG12-ATG16L1 complex at the bacterial vacuolar membrane via secretion of the
84 effector SopF, which blocks ATG16L1 association with vacuolar ATPases (Xu et al.,
85 2019b). Despite its ability to interfere with autophagy, infected host cells still
86 recognize 10-20% of cytosolic *S.typhimurium* and subject this sub-population to
87 lysosomal degradation via mechanisms involving direct recognition of either the
88 bacterial surface (Huang and Brumell, 2014; Stolz et al., 2014) or damaged
89 phagocytic membranes (Fujita et al., 2013; Thurston et al., 2012).

90 Compared to *S.typhimurium*, *S.flexneri* is not characterized by a vacuolar life
91 cycle, but instead resides in the host cytoplasm. *S.flexneri* effector proteins IcsB and
92 VirA are capable of completely inhibiting autophagic recognition to permit replication
93 in the host cytosol (Liu et al., 2018; Ogawa et al., 2005). In response, the host cell
94 attempts to further counteract *S.flexneri* infection via diverse mechanisms, such as
95 coating bacterial cell surfaces with guanylate-binding proteins (GBPs) (Li et al., 2017;
96 Wandel et al., 2017) or sequestering bacteria in septin cage-like structures to restrict
97 their motility (Mostowy et al., 2010). To reveal these mechanisms, cell-based studies
98 have largely utilized attenuated variants (e.g. IcsB or IcsB/VirA double mutants of
99 *S.flexneri*) or strains that inefficiently colonize the host cytosol (e.g. *S.typhimurium*
100 which express SopF). Thus, observations from *in vivo* genetic models must be

101 reconciled with observations made in cell-based systems to fully describe the roles of
102 autophagy in antimicrobial immunity. Importantly, there is a lack of understanding of
103 how autophagy contributes to immunity against non-attenuated (wild type) cytosolic
104 pathogens. This insight is especially lacking in relevant cell types, such as
105 macrophages that constitute a physiologically relevant niche for the expansion of
106 *S.flexneri* (Ashida et al., 2015).

107 In this study we investigated the role of macrophage ATG16L1 in response to
108 infection by wild type *S.flexneri* (strain M90T). Surprisingly, we observed that loss of
109 *Atg16l1* in BMDMs enhanced *S.flexneri* elimination in culture, as well as by mice
110 lacking ATG16L1 in the myeloid compartment *in vivo* (*Atg16l1-cKO*). We utilized
111 multiplexed quantitative proteomics to characterize total protein, phosphorylation and
112 ubiquitination changes in wild type (WT) and ATG16L1-deficient (cKO) bone marrow-
113 derived macrophages (BMDMs) either uninfected or infected with *S.flexneri*.
114 Quantifying global protein levels along with site-specific post-translational
115 modifications (PTMs) provided a comprehensive catalogue of basal differences
116 between WT and cKO BMDMs and the dynamic response of each to infection. As
117 expected, profound differences were observed for components in the autophagy
118 pathway, as well as proteins involved in cell death, innate immune sensing and NF-
119 κB signaling. Interestingly, a cluster of proteins emerging from the proteomics data
120 implicated the basal oxidative stress response as a key difference between control
121 and ATG16L1-deficient BMDMs. In particular, significant accumulation of the
122 SLC7A11 subunit of a sodium-independent cystine-glutamate antiporter (XCT),
123 critical for the generation of glutathione (GSH) used in detoxification of ROS and lipid
124 peroxides, was noteworthy in cKO cells. This coincided with basal elevation of
125 cytosolic ROS in cKO BMDMs, thus providing an explanation for the sustained
126 viability and antimicrobial capacity of ATG16L1-deficient macrophages. Furthermore,
127 increased cytosolic ROS caused by pharmacological XCT inhibition enhanced
128 *S.flexneri* clearance by WT BMDMs, recapitulating cKO phenotypes. Taken
129 together, this study offers a comprehensive, multidimensional catalogue of proteome-
130 wide changes in macrophages following infection by an enteric cytosolic pathogen,
131 including key nodes of cell-autonomous immunity regulated by autophagy. Our
132 findings demonstrate that ATG16L1 tunes antimicrobial immunity against cytosolic
133 pathogens via the oxidative stress response, and that pharmacological modulation of

134 this pathway represents a novel strategy towards enhanced elimination of cytosolic
135 pathogens.

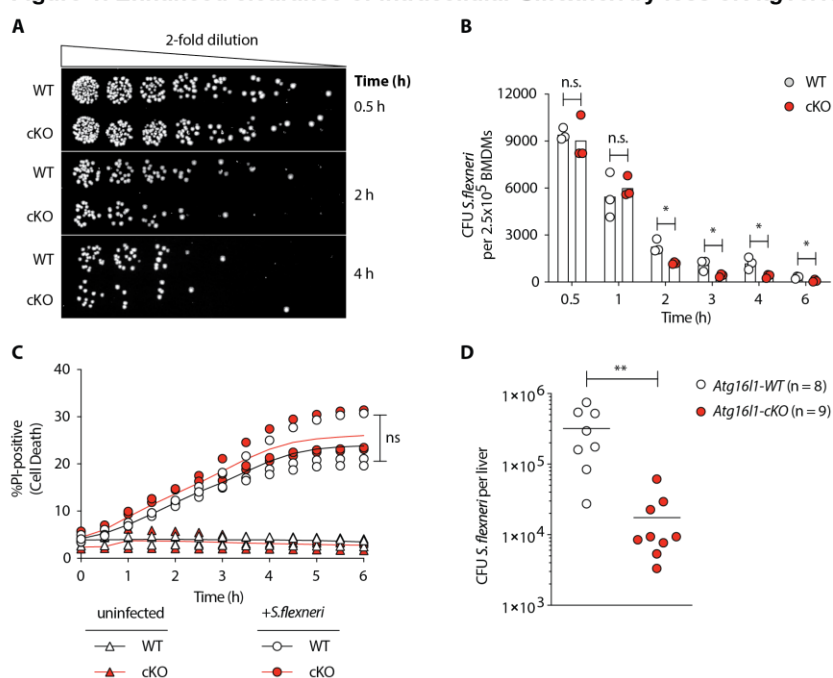
136

137 Results

138 Enhanced clearance of intracellular *S.flexneri* by loss of *Atg16l1*.

139 Recent studies have identified that defective autophagy in macrophages
140 enhances multiple inflammatory signaling responses to promote antimicrobial
141 immunity (Lim et al., 2019; Martin et al., 2018; Samie et al., 2018; Wang et al., 2020).
142 Given these observations, we wanted to explore whether loss of *Atg16l1* affects
143 killing of the wild type, invasive, intracellular pathogen *Shigella flexneri* strain M90T
144 (*S.flexneri*). To test this, bone marrow-derived macrophages (BMDMs) from either

Figure 1. Enhanced clearance of intracellular *S.flexneri* by loss of *Atg16l1*.



(A) Representative serial dilutions from gentamycin protection assays following *S.flexneri* M90T infection of WT or cKO BMDMs at the indicated timepoints. (B) Comparison of colony forming units (CFUs) per well from three independent infection experiments using BMDM preparations from three different *Atg16l1*-WT or *Atg16l1*-cKO mice. ns, non-significant; 2h * P = 0.01, 3h * P = 0.03, 4h * P = 0.02, 6h * P = 0.03, multiple t-test comparison. (C) Percentage of propidium iodide (PI)-positive cells during time-course infection of WT or cKO BMDMs with *S.flexneri* M90T. Graph represents individual values from three independent experiments using three different BMDM preparations. ns, non-significant. (D) Liver bacterial load 24 hours following intravenous injection of *Atg16l1*-WT or *Atg16l1*-cKO mice with *S.flexneri* M90T. Graph shows data from a representative experiment out of four different experiments as log10 CFU count per liver in indicated number of mice, ** P = 0.0031. Outliers removed using ROUT (Q = 1%) method.

145 control (*Atg16l1*-WT) or mice lacking ATG16L1 in the myeloid compartment (*Atg16l1*-
146 cKO) were subjected to the gentamycin protection assay that enables quantification
147 of intracellular bacteria by enumerating colony forming units (CFUs). We first
148 determined the kinetics of *S.flexneri* killing by following BMDM infection over six
149 hours (MOI 5). Compared to wild type (WT) controls, ATG16L1-deficient BMDMs
150

151 (cKO) demonstrated accelerated bacterial clearance starting at two hours post-
152 infection (Figure 1A and 1B). Previous studies demonstrated enhanced sensitivity of
153 autophagy-deficient cells to programmed cell death following engagement of cytokine
154 receptors and microbial ligands (Lim et al., 2019; Matsuzawa-Ishimoto et al., 2017;
155 Orvedahl et al., 2019). Thus, BMDM viability was measured in parallel by quantifying
156 the propidium iodide (PI)-positive population via live-cell imaging. WT and cKO
157 BMDMs displayed similar cell death kinetics over the time course of infection,
158 indicating that accelerated *S.flexneri* killing was not driven by enhanced cell death,
159 but potentially by other cytosolic factors in cKO BMDMs (Figure 1C).

160 To corroborate this finding *in vivo*, control and *Atg16l1-cKO* mice were
161 infected with the *S.flexneri* via tail vein injection and CFUs enumerated from hepatic
162 lysates. Myeloid-specific loss of *Atg16l1* resulted in a markedly decreased bacterial
163 burden 24 hours post-infection (Figure 1D). Taken together, these observations
164 establish that ATG16L1 restrains macrophage immunity against cytosolic bacteria
165 such as *S.flexneri*.

166

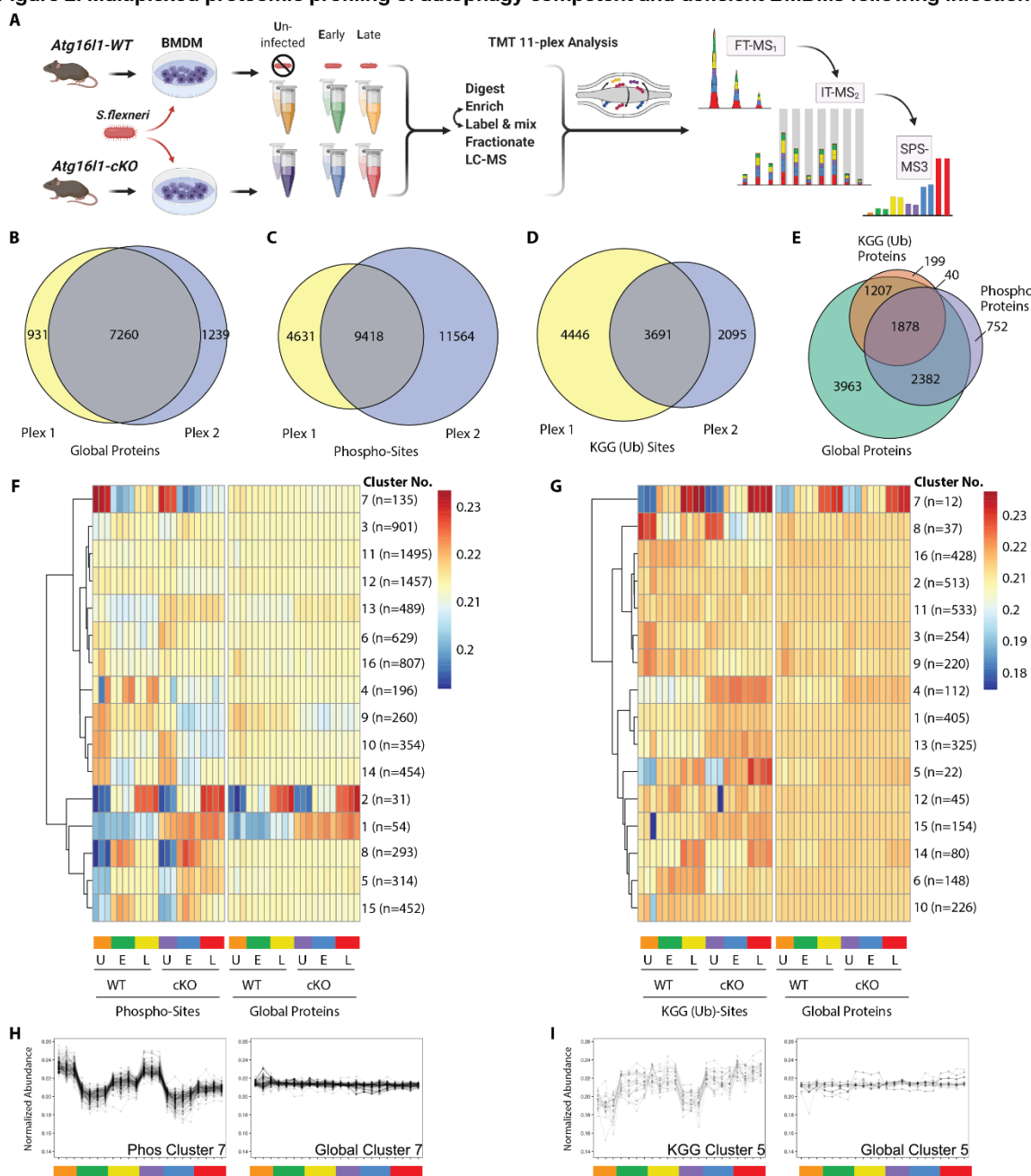
167 **Multiplexed proteomic profiling of autophagy competent and deficient BMDMs 168 following infection.**

169 To reveal factors that may drive enhanced *S.flexneri* killing in ATG16L1-
170 deficient BMDMs, we characterized changes in global proteome and post-
171 translational modifications (PTMs) in proteins between WT and cKO BMDMs. To that
172 end, we applied tandem mass spectrometry coupled with tandem mass tagging
173 (TMT) 11-plex isobaric multiplexing. Cell lysates were prepared from WT and cKO
174 BMDMs that were either uninfected (U) or infected at early (E; 45-60min) or late (L;
175 3-3.5h) time-points with *S.flexneri* (MOI 5). Cumulatively, two 11-plex experiments
176 were performed with uninfected samples represented in biological triplicates and
177 infected samples represented in biological quadruplicates (see Methods for details)
178 (Figure 2A). Data were acquired using the recently established SPS-MS3 approach
179 wherein dedicated MS3 scan events are collected from fragment ion populations
180 representing a mixture of the 11 samples and used to report the relative abundance
181 of each peptide feature per channel (McAlister et al., 2014; Ting et al., 2011).

182 For global proteome profiling, quantitative data was obtained from >103,700
183 unique peptides mapping to 9430 proteins. From the PTM enriched samples,
184 quantitative data were obtained for >25,600 unique phosphorylation sites (5052

185 proteins) and >12,400 unique KGG (Ub) sites (3324 proteins). When considering only
 186 features bearing data in both 11-plexes, the final dataset contained 22 channels of

Figure 2. Multiplexed proteomic profiling of autophagy competent and deficient BMDMs following infection.



(A) Schematic representation of multiplexed proteomic profiling of macrophages during *S. flexneri* infection. (B-D) Venn diagrams show overlapping quantitative data collected in Plex1 and/or Plex2 for (B) Global Proteins, (C) Phosphorylation sites and (D) KGG (Ub) sites. (E) Venn diagram displays an overlap of quantitative data for Phospho- and KGG (Ub) sites with respect to the Global Proteins quantified. (F and G) Heatmaps displaying K-means clustered quantitative data for (F) Phospho-sites and (G) KGG (Ub) sites relative to their corresponding Global Proteins. Note that Global Protein clustering differs between panels F and G based on the proteins from which PTMs were quantified. (H and I) Line plots showing representative clusters from the Heatmaps above. Phospho Cluster 7 (panel H) and KGG (Ub) Cluster 5 (panel I) each show PTM profiles that diverge from their corresponding Global Protein measurements. Proteins and PTMs making up each cluster are presented in Table S1.

187 quantitative data for 7260 proteins (i.e. global proteome), 9418 phosphorylation sites
 188 and 3691 KGG modification sites (Figure 2B-D). As expected, ~90% of the post-

190 translationally modified peptide spectral matches derived from proteins that were also
191 identified and quantified in the global proteome dataset (Figure 2E). Both within and
192 between plexes, peptide and protein level quantitative data were highly reproducible
193 with Pearson correlations ranging from 0.96-0.99 (Figure S1A). Phosphorylation and
194 KGG profiling data were subjected to K-means clustering, each paired with the
195 corresponding global proteome data. Heatmap representations revealed clusters of
196 PTM changes that occur in genotype and/or infection dependent manners (Figure 2F
197 and 2G). A subset of these clusters comprised PTMs whose quantitative profiles
198 mirrored that of the underlying protein level due to altered protein expression or
199 stability (e.g. Phospho Clusters 1-2 in Figure 2F and S1B; KGG Cluster 7 in Figure
200 2G and S1C). In contrast, other clusters displayed PTM profiles that diverged from
201 their underlying proteins (e.g. Phospho Cluster 7 in Figure 2F and 2H; KGG Cluster 5
202 in Figure 2G and 2I). The composition of PTMs and proteins comprising each cluster
203 are available in Table S1.

204 Interrogation of the uninfected datasets revealed differences between the
205 genotypes on the global protein level. Consistent with previous observations (Samie
206 et al., 2018), cKO BMDMs showed upregulation in autophagy receptors, such as
207 SQSTM/p62 and ZBP1 (Figure S2A). In the phosphorylation and KGG datasets,
208 interesting observations amongst others concerned elevated phosphorylation of
209 ubiquitin (RL40) at serine (S) 57 and ubiquitination of FIS1 at lysine (K) 20, which are
210 involved in endocytic trafficking (Lee et al., 2017; Peng et al., 2003) and
211 mitochondrial and peroxisomal homeostasis (Bingol et al., 2014; Koch et al., 2005;
212 Zhang et al., 2012), respectively (Figure S2B and S2C).

213 Interrogation of the infected datasets revealed the dynamic nature of the
214 macrophage response to infection. For example, global proteome analysis revealed
215 broad changes in pro-inflammatory cytokines and chemokines at early (GROA), late
216 (CXL10, IL1A, IL1B) or both (CCL2, TNFA) time-points, as well as marked changes
217 in several key cell surface receptors (Figure S2D, S3A and S3B). Time-dependent
218 changes were also observed for components of innate immune signaling that
219 intersect with the ubiquitin pathway (PELI1), kinase-phosphatase signaling
220 (DUS1/Dusp1) and GTP/GDP signaling (GBP5) (Figure S3C). For phosphorylation,
221 notable examples included tyrosine (Y) 431 of the PI3-kinase regulatory subunit
222 (P85A) and S379 of the interferon regulatory factor (IRF3) (Figure S2E). In the case
223 of ubiquitination, marked effects are seen for a selective autophagy receptor

224 Tax1BP1 (TAXB1_K618) and an E3 ubiquitin ligase Pellino (PELI1_K202) (Figure
225 S2F), both of which have defined roles at the intersection of cell death and innate
226 immune signaling (Choi et al., 2018; Gao et al., 2011; Parvatiyar et al., 2010).

227 It is beyond of the scope of this study to describe these in-depth proteomic
228 observations. Therefore, we developed interactive Spotfire Dashboards as a
229 resource to facilitate discoveries in cellular pathways of interest by other
230 investigators. These can be accessed at the following URL:
231 <https://info.perkinelmer.com/analytics-resource-center>.

232

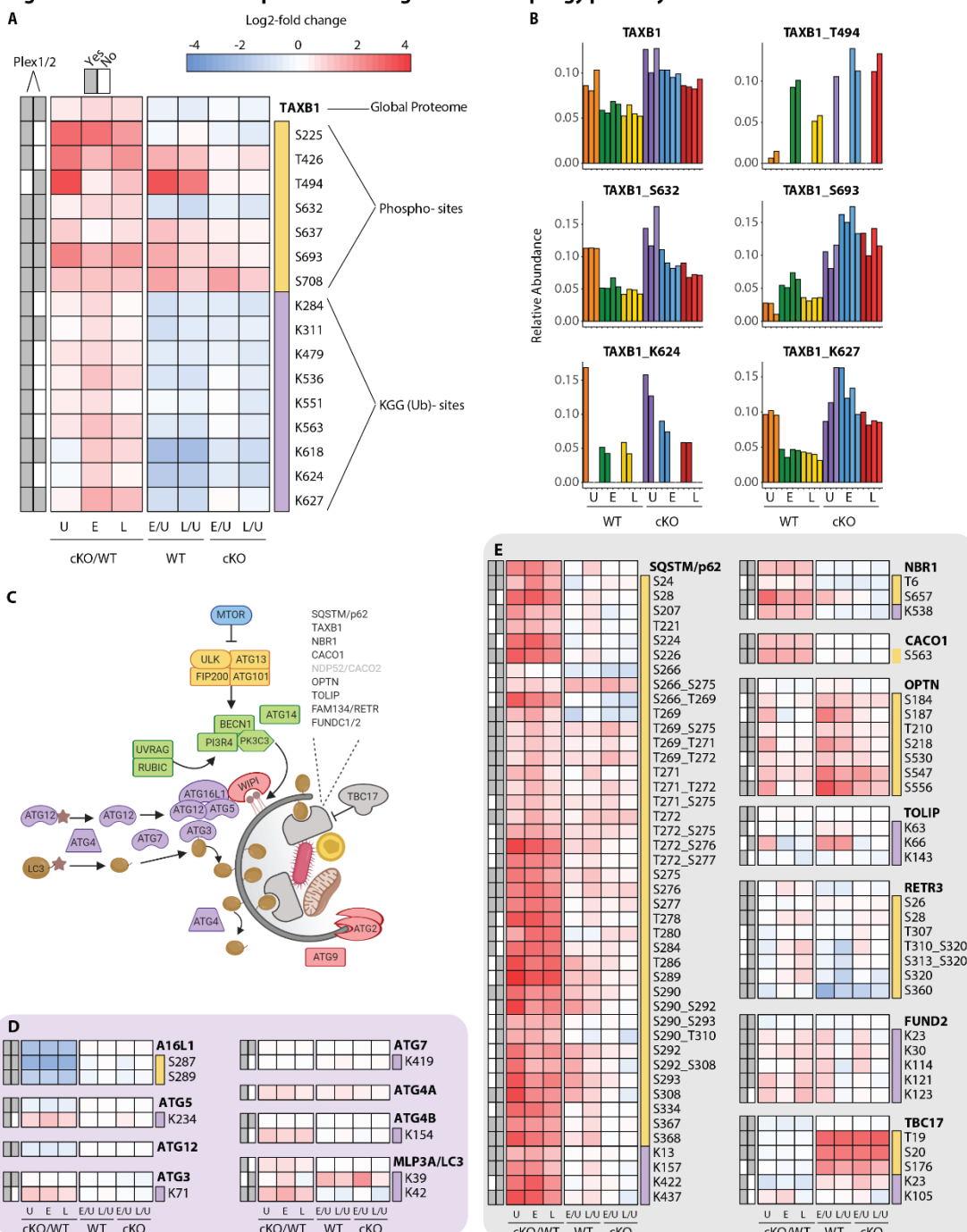
233 **Characterizing PTMs of autophagy proteins and inflammatory signaling nodes 234 revealed by loss of *Atg16l1* and infection.**

235 To effectively integrate data for each protein within a single consolidated view,
236 heatmaps were assembled to show the proteome level change immediately adjacent
237 to any PTMs that were identified in the phospho- and KGG-enriched samples. In the
238 example for selective autophagy receptor Tax1bp1 (TAXB1), heatmaps depict
239 relative abundance of features present in one or both experiments (Plex1 and/or
240 Plex2) (Figure 3A). Comparisons of interest include cKO versus WT for uninfected,
241 early and late infection time-point samples. For TAXB1, these show that the global
242 protein level is elevated upon *Atg16l1* deletion, as are a number of individual
243 phosphorylation and ubiquitination sites including those quantified in one (e.g. T494,
244 K624) or both plexes (e.g. S632, S693, K627). Additional comparisons call out time-
245 dependent differences between infected and uninfected conditions for each genotype
246 – namely early versus uninfected (E/U) and late versus uninfected (L/U). For TAXB1,
247 certain PTMs such as phosphorylation at S632 and ubiquitination at K624 and K627
248 track with the protein, while other PTMs such as phosphorylation at threonine (T) 494
249 and S693 display time-dependent changes that diverge from the underlying protein
250 level (Figure 3A). Shown individually, histograms depict the same information for
251 relative abundance of TAXB1 and its specific PTMs (Figure 3B). Therefore, the
252 heatmaps provide a succinct visual representation of all detected changes in protein
253 and PTM abundance.

254 One pathway where we expected to see marked proteome and PTM level
255 changes upon infection was in autophagy (Figure 3C and S4). We confirmed
256 genotype-dependent effects on each component of the ATG5-ATG12-ATG16L1 E3
257 ligase-like complex that conjugates LC3 (MLP3A) to phosphatidylethanolamine

258 (Figure 3D). Only modest changes were seen in the core autophagy machinery
259 following infection, with the most notable effects being differential phosphorylation of
260 FIP200 (RBCC1),

Figure 3. Characterization of proteomic changes in the autophagy pathway.



(A) Heatmap representation of log₂ fold changes for global proteome (unmarked), phospho-(yellow section) or KGG (Ub)- sites (purple section) measurements made for TAXB1. Data are shown for features quantified from uninfected (U) WT and cKO BMDMs or cells infected at early (E) or late (L) timepoints with *S. flexneri*. Log₂ transformed ratios are shown for contrasting genotypes (cKO/WT) at each infection timepoint (U, E, L) on the left and between infection timepoints (E/U and L/U) within each genotype on the right. Grey boxes denote quantification of the feature in Plex1 and/or Plex2. Modification sites on TAXB1 denote the modified amino acid (S/T/Y/K) and residue number. (B) Bar graphs showing the relative abundance of TAXB1 global protein and representative phospho- and KGG (Ub)- sites in each of the six conditions. Note that TAXB1_K624 (Plex1) and TAXB1_T494 (Plex2) represent data collected only in a single Plex, with the relative abundance of TMT reporter ions summing up to 1.0. (C) Schematic representation of macro-autophagy & selective autophagy machinery. (D and E) Heatmap representations of E1/E2/E3-like pathway components responsible for conjugating LC3 (MLP3A) to regulate autophagosome membrane elongation (D) and selective autophagy receptors (E). The background shading for each panel corresponds to the functional color coding of proteins in the pathway schematic shown in (C).

262 ATG2B, and VPS15/p150 (PI3R4) (Figure S4C-E). More substantial effects were
263 seen for phosphorylation events on autophagy receptors such SQSTM/p62,
264 Optineurin (OPTN) (Figure 3E) and TAXB1 (Figure 3A). In the case of p62, singly
265 and multiply phosphorylated forms of T269, T271, T272, S275/6, S277 were elevated
266 in ATG16L1-deficient macrophages, most notably at the early timepoint post-
267 infection. S28 phosphorylation of p62 was previously described to regulate activation
268 of the antioxidant response (Xu et al., 2019a). Interestingly, we detected a substantial
269 increase in basal S28 phosphorylation in cKO BMDMs, indicating that ATG16L1
270 deficiency may impact oxidative stress (Figure S4F).

271 Our PTM datasets showed dynamic regulation of a range of inflammatory
272 signaling components by infection as well as autophagy (Figure S5). For example,
273 we detected ubiquitination of K278 of NEMO (Figure S5F), consistent with increased
274 LUBAC activity (Tokunaga et al., 2009). Interestingly, the global proteome data
275 reported a peptide with the sequence GGMQIFVK that is derived from linear
276 polyubiquitin chains formed by the LUBAC complex. This linear ubiquitin peptide was
277 elevated upon infection in both WT and cKO BMDMs (Figure S3D), further
278 supporting increased E3 ubiquitin ligase activity of LUBAC. As noted above, TAXB1
279 phosphorylation was induced upon infection at a number of sites (Figure 3A). These
280 changes in TAXB1 correlated with numerous elevated PTMs of the A20 (TNAP3)
281 deubiquitinase, a protein whose anti-inflammatory activity modulates NF- κ B signaling
282 (Figure S5C). Interestingly, phosphorylation at S693 of TAXB1 is important for the
283 assembly of TNAP3-containing complex and negative regulation of NF- κ B signaling
284 (Shembade et al., 2011) (Figure 3A).

285 We also identified notable changes across numerous components implicated
286 in pathogen sensing such as TLRs, RLRs, NLRs and STING/cGAS (Supplementary
287 Figure S6A and S6B). Our datasets confirm numerous previously demonstrated
288 PTMs that occur in response to infection, such as elevated phosphorylation of RIPK1
289 at S321 (Figure S5E), XIAP at S429 or IRF3 on multiple sites (Figure S6D and S6E).
290 Similar effects were observed for ABIN1 (TNIP1), which showed minimal changes in
291 global protein levels, but elevated ubiquitination at multiple lysines including K360,
292 K402, K480 at both timepoints and higher levels in cKO than WT (Figure S5F).
293 Caspase-8 ubiquitination was elevated at K169 in both WT and cKO early post-
294 infection, but was sustained through the late timepoint only in ATG16L1-deficient
295 BMDMs (Figure S5G). Within the ubiquitin pathway, E3 ubiquitin ligases including

Table 1. Novel post-translational modifications in specific autophagy, innate sensing, inflammatory signaling and cell death pathways revealed by TMT-MS of BMDMs following *S.flexneri* infection.

Autophagy		
Protein name	Post-translational modification	
	pSTY/Phosphorylation	KGG/Ubiquitination
ATG5		K234
MLP3A/LC3		K39
TAX1BP1	T426, T494	K284, K311, K536, K551, K624
P62/SQSTM1	T280, S292, S308	
NBR1	T6	
FUND2		K114, K121
TBC17	S176	K105
RBCC1/FIP200	T642	
PI3R4/VPS15	S903, T904	
RUBIC	S252, S552, S554	
ATG2B	S401	T1570
Innate sensing		
Protein name	Post-translational modification	
	pSTY/Phosphorylation	KGG/Ubiquitination
DDX58/RIG-I		K256
MAVS	Y332	
CGAS		K55
TLR4		K692
MYD88	S136	
IRAK2	S175, T587, S615	
IRAK3		K60, K163, K392
IRAK4	T133, S134, S175_S186	
TBK1	S509	
IRF3	T126, S130	
IRF7	S227, T277	
IFIT1	S272, S296	K89, K117, K123, K406, K451
IFIT2		K41, K61, K158, K291
IFIT3	S327, S333	K246, K252, K266, K396
ISG15	K30	
Inflammatory signaling, cell death		
Protein name	Post-translational modification	
	pSTY/Phosphorylation	KGG/Ubiquitination
TNFR1B/TNFR2		K300
M3K7/TAK1	S331	
TAB2	S353, T376, S584	
TRAF1		K120
TRAF2		K194
IKBz	T188	K5, K120, K132
NFKB1		K275
REL	S321	
RNF31/HOIP	S441, S973	K911
TNAP3/A20	S217, T567, S622, S730	K31, K213
TNIP1/ABIN1	S601	K288, K317, K386
TNIP2/ABIN2	T194, S196	
CASP8	S60	K33, K274
CFLAR/cFLIP		K175, K390
RIPK1		K429
RIPK2	S183, S381	K369
RIPK3	S173, S177, S254, T386, T392, T398, T407	K145, K230, K298

296 HOIP (RNF31), TRAF2, and Pellino (PELI1) showed marked infection dependent
 297 changes at the level of phosphorylation (e.g. RNF31_S445) and ubiquitination (e.g.
 298 PELI_K202 early, TRAF2_K313 late) (Figure S5C).

299 Cross-referencing all highlighted PTMs with PhosphoSitePlus® revealed that
300 ~60% of PTMs were previously identified in distinct large-scale proteomic screens
301 without assigning a specific biological role, but only 15% of PTMs have been studied
302 in connection to a biological function (Tables S2 and S3). This analysis also revealed
303 that nearly 25% of PTMs in autophagy, innate sensing, inflammatory and cell death
304 signaling identified in our study appear to be novel (summarized in Table 1).

305

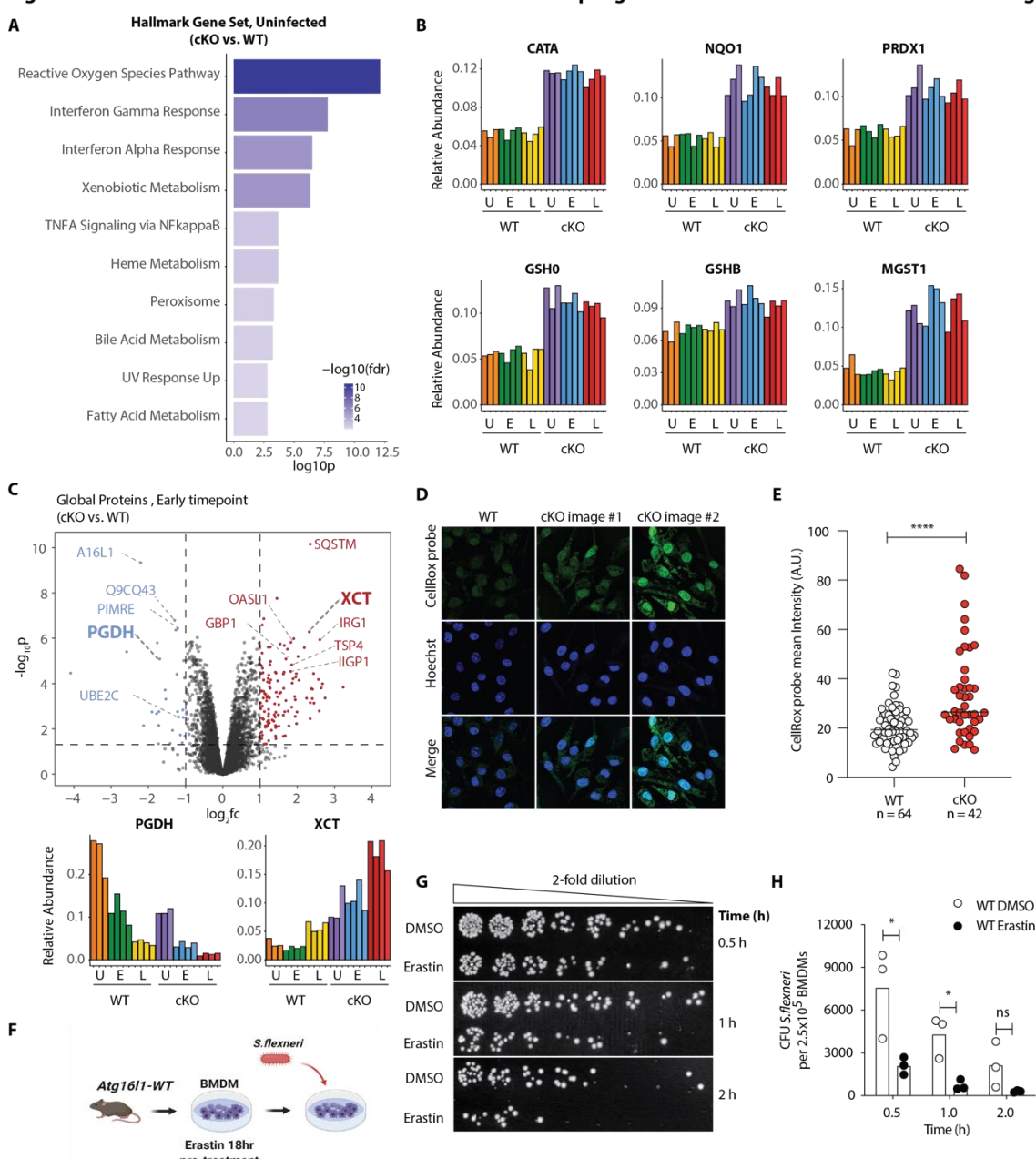
306 **Elevated oxidative stress in ATG16L1-deficient macrophages contributes to
307 accelerated bacterial killing.**

308 To reveal cellular processes overrepresented in cKO BMDMs in an unbiased
309 manner, we leveraged the deep coverage of the global proteome by TMT-MS and
310 performed gene set enrichment analysis (GSEA). Unexpectedly, this analysis
311 revealed a strong enrichment of the components of reactive oxygen species (ROS)
312 pathway (Figure 4A and Table S4 for protein set terms). Further assessment of the
313 components of this gene ontology term revealed critical regulators of redox
314 homeostasis that were increased in uninfected cKO BMDMs at steady state relative
315 to WT (Figure 4B). This group of proteins included several factors involved in
316 glutathione (GSH) synthesis, such as the glutamate-cysteine ligase regulatory
317 subunit (GSH0/Glcml) and GSH synthetase (GSHB/Gss), and GSH regeneration,
318 such as microsomal glutathione S-transferase (MGST1) and NAD(P)H
319 dehydrogenase 1 (NQO1). Additionally, several ROS converting enzymes including
320 catalase (CATA) and peroxiredoxin 1 (PRDX1) were also elevated in cKO BMDMs at
321 steady state. Furthermore, a subset of these redox regulators changed abundance
322 upon *S.flexneri* infection. For example, prostaglandin dehydrogenase 1 (PGDH)
323 displayed a time dependent decrease upon infection that was accentuated in cKO
324 versus WT, consistent with its known susceptibility to ROS (Wang et al., 2018).
325 Conversely, levels of the cysteine-glutamate antiporter SLC7A11 (XCT) (Conrad and
326 Sato, 2012; Sato et al., 1999) exhibited a significant increase in cKO BMDMs
327 following infection (Figure 4C). Thus, ATG16L1 deficiency and *S. flexneri* infection
328 might each independently elevate ROS levels, with ATG16L1 deficiency further
329 driving a compensatory increase in the lipid ROS regulatory pathway during infection
330 to maintain macrophage viability.

331 To determine if ATG16L1-deficient BMDMs are exposed to higher oxidative
332 stress, we first used a fluorogenic probe (CellRox green) that enables measurement

333 of oxidative stress by confocal fluorescence microscopy. Interestingly, despite

Figure 4. Elevated oxidative stress in ATG16L1-deficient macrophages contributes to accelerated bacterial killing.



(A) Gene set enrichment analysis (GSEA) of global proteome data showing cellular processes overrepresented in uninfected cKO over WT BMDMs. (B) Bar graphs showing the relative abundances for selected proteins involved in redox regulation and detoxifying reactive oxygen species. (C) Volcano plot of global protein changes at early infection timepoint between the genotypes. Proteins enriched in cKO and WT BMDMs are highlighted in red and blue, respectively. Bar graphs showing the cumulative effects of genotype and infection on PGDH and XCT protein levels. (D) Representative images from experiments shown in (E) demonstrating CellRox probe intensity, Hoechst nuclear staining and merged images. (E) Quantification of CellRox green mean intensity in WT and cKO BMDMs. Graph shows single cell data from a representative experiment (n = 3). Unpaired t test *** P < 0.0001. (F) Schematic representation of infection experiment using pre-treatment of BMDMs with Erastin. (G) Representative serial dilutions from gentamycin protection assays following *S. flexneri* M90T infection of WT BMDMs in the presence of DMSO or Erastin (4 $\mu\text{g}/\text{ml}$) at the indicated timepoints. Erastin-treated WT BMDMs were pre-treated with Erastin for 18 hours prior infection (T = 0). (H) Comparison of CFUs from three independent infection experiments using BMDM preparations from three different Atg16l1-WT mice. ns, non-significant; 0.5 h * P = 0.04, 1 h * P = 0.01.

334
335 upregulation of numerous redox regulatory factors, CellRox probe intensity was

336 significantly higher in cKO BMDMs (Figure 4D and 4E). In line with these
337 observations, we also detected an increase in the ratio between oxidized versus
338 reduced GSH (GSSH/GSH) in cKO BMDMs (Figure S7A-C). Given the central role of
339 autophagy in mitochondrial turnover, we assessed mitochondrial morphology and
340 respiration as a likely source of oxidative damage in uninfected cKO BMDMs (Figure
341 S7D and S7E). However, no mitochondrial defect could be identified; this warrants
342 further investigation into the underlying mechanism(s) of elevated oxidative stress in
343 ATG16L1-deficient BMDMs.

344 Taken together, observations that cKO BMDMs are burdened with higher
345 oxidative stress suggest that elevated ROS in these cells mandate upregulation of
346 redox homeostasis factors in order to maintain viability (Tal et al., 2009). We thus
347 asked whether accumulation of cytosolic ROS could be recapitulated by suppression
348 of glutathione import in wild type macrophages. BMDMs were pre-treated with
349 Erastin, a small molecule inhibitor of XCT, which diminishes the levels of reduced but
350 not oxidized GSH in cells (Dixon et al., 2012). Time-course treatment demonstrated
351 that cKO BMDMs are slightly more sensitive to Erastin after prolonged incubation,
352 consistent with a basal elevation in cellular ROS (Figure S7F). Interestingly, 24-hour
353 Erastin treatment of WT BMDMs phenocopied a steady-state ROS level in cKO cells,
354 while no further increase in ROS was observed in cKO BMDMs treated with Erastin
355 (Figure S7G). We hypothesized that induction of cellular ROS in WT BMDMs by
356 pharmacological inhibition of XCT should phenocopy the accelerated *S.flexneri*
357 clearance seen in cKO cells. To test this, WT BMDMs were pre-treated with Erastin
358 for 18 hours prior infection and Erastin was maintained throughout the experiment
359 (Figure 4F). Importantly, Erastin treatment did not increase WT BMDM cell death
360 within the time-course (Figure S7H). However, Erastin-treated WT BMDMs showed
361 enhanced elimination of *S.flexneri* following infection (Figure 4G and 4H),
362 demonstrating that elevated oxidative stress in WT BMDMs accelerates killing of
363 *S.flexneri*, consistent with enhanced microbicidal capacity of ATG16L1-deficient
364 BMDMs.

365

366 **Discussion**

367 Emerging insights from genetic mouse models have revealed that loss of
368 *Atg16l1* in the immune and epithelial compartments lowers the threshold for an
369 inflammatory response (Cadwell et al., 2010; Hubbard-Lucey et al., 2014; Lim et al.,

370 2019; Matsuzawa-Ishimoto et al., 2017). Consistently, deletion of canonical
371 autophagy genes in the innate and adaptive immune compartments have
372 demonstrated enhanced pathogen clearance (Marchiando et al., 2013; Martin et al.,
373 2018; Samie et al., 2018; Wang et al., 2020) as well as tumor control *in vivo* (Cunha
374 et al., 2018; DeVorkin et al., 2019). These observations have prompted a re-
375 evaluation of antimicrobial selective autophagy (xenophagy) to better understand
376 how loss of core autophagy genes impacts cell-autonomous innate immunity against
377 pathogenic intracellular bacteria.

378 In this study we show that macrophages deficient in ATG16L1 demonstrate an
379 accelerated killing of *Shigella flexneri* *in vitro* and *in vivo*. To identify mechanisms
380 behind this phenotype we employ isobaric multiplexing using the TMT technology,
381 which emerged as being capable of near-comprehensive characterization of the
382 global proteome (Lapek et al., 2017). When isobaric multiplexing methods are
383 coupled with enrichment, it enables quantification of post-translational modifications
384 on thousands of individual proteins (Rose et al., 2016). This method is ideally suited
385 for interrogation of a complex response, such as infection of a host cell with an
386 intracellular pathogen, where the diversity of downstream changes does not lend
387 themselves to candidate approaches involving immunoblotting.

388 Our approach identifies multiple novel PTMs in components of inflammatory
389 cytokine signaling, innate sensing and the core autophagy machinery that emerge as
390 a consequence of *S.flexneri* infection. The comparison of early and late infection
391 time-points shows a complex dynamic in the stability of PTMs as well as total protein
392 abundance. The comparison of wild type versus ATG16L1-deficient BMDMs further
393 reveals critical nodes in each of the above pathways that are under regulatory control
394 by autophagy. The PTMs listed in Table 1, S2 and S3 represent a sizeable fraction of
395 the relevant post-translational changes that occur in macrophages during infection
396 and/or loss of autophagy. It is beyond the scope of a single study to interrogate these
397 changes comprehensively; we encourage groups to utilize this study as a resource to
398 explore PTMs in their pathway(s) of interest. We have provided interactive, web-
399 accessible Spotfire Dashboards to enable user interrogation of the Global Proteome,
400 Phospho-proteome, and the Ubiquitinome (KGG) datasets
401 (<https://info.perkinelmer.com/analytics-resource-center>).

402 Our study reveals that basal accumulation of cellular ROS in cKO BMDMs
403 enforces a compensatory increase in antioxidant responses exemplified by elevated

404 protein abundances of key components of the glutathione synthesis machinery. This
405 permits cellular viability under relatively elevated cytosolic ROS levels, which in turn
406 suppresses *S.flexneri* expansion in BMDMs. However, overall macrophage fitness is
407 likely compromised owing to a shift in the basal redox pathway set-point, and the
408 accelerated clearance of *S.flexneri* observed in livers of *Atg16l1-cKO* mice may also
409 contribute to inflammation-mediated loss of the hepatic myeloid cell niche *in vivo*.
410 Pharmacological depletion of GSH phenocopies genetic loss of *Atg16l1*, accelerating
411 *S.flexneri* clearance in wild type cells. These findings should prompt further
412 investigation of autophagy in the intestinal epithelium, another key cellular niche for
413 virulent *S.flexneri*. It is important to note that there are no viable murine models of
414 enteric *S.flexneri* infection; development of model systems that permit intestinal
415 infection while maintaining adequate inflammatory responses will be key in
416 reconciling cell-based versus *in vivo* findings.

417 Our study provides the most comprehensive multiplexed proteomic analysis of
418 the macrophage response to a cytosolic enteric pathogen to date. This novel
419 resource will be of broad utility to the study of myeloid signal transduction, host-
420 pathogen interaction and innate immunity.

421 **Materials and Methods**

422 **Mice.** All animal experiments were performed under protocols approved by the
423 Genentech Institutional Animal Care and Use Committee (Protocol ID 17-2842).
424 Generation of myeloid-specific deletion of *Atg16l1* was achieved by crossing *LysM-*
425 *Cre+* mice with *Atg16l1*^{loxp/loxp} mice and was described previously (Murthy et al.,
426 2014). All mice were bred onto the C57BL/6N background. All *in vivo* experiments
427 were performed using age-matched colony controls.

428 **Bacterial strains and culture.** *Shigella flexneri* 5a strain M90T used in this study
429 was obtained from ATCC (ATCC® BAA-2402™). *Shigella flexneri* strain M90T $\Delta mxiE$
430 used in this study was obtained from a *S. flexneri* mutant collection (Sidik et al.,
431 2014). Frozen bacterial stocks were streaked onto tryptic soy agar (TSA) plates and
432 grown at 37 °C overnight. Plates were kept at 4 °C for up to 2 weeks.

433 **Bone marrow-derived cells isolation.** Femurs and tibias were collected aseptically.
434 After removing most of the muscle and fat, the epiphyses were cut and bones were
435 placed into PCR tubes individually hung by the hinge into a 1.5 ml Eppendorf. The
436 bone marrow was flushed by short centrifugation at 10,000 rpm for 30 seconds. Red
437 blood cells were lysed with RBC lysis buffer (Genentech) by incubating for 5 minutes
438 at RT. Cells were then pelleted and resuspended in BMDM media [high glucose
439 Dulbecco's Minimum Essential Media (DMEM) (Genentech) + 10% FBS (VRW,
440 custom manufactured for Genentech) + GlutaMAX (Gibco, 30050-061) + Pen/Strep
441 (Gibco, 15140-122) supplemented with 50 ng/ml recombinant murine macrophage-
442 colony stimulating factor (rmM-CSF, Genentech)] and plated in 15-cm non-TC
443 treated dishes for 5 days (Petri dish, VWR, 25384-326). Fresh BMDM media was
444 added on day 3 without removal of original media. On day 5, macrophages were
445 gently scraped from dishes, counted and re-plated on TC-treated plates of the
446 desired format for downstream assays in fresh BMDM media. After overnight culture
447 in BMDM media, assays were performed on day 6 BMDMs.

448 **BMDM infections in 24-well plates.** BMDMs isolated from control *LysM-Cre+* or
449 *LysM-Cre+ Atg16l1*^{loxp/loxp} mice were plated at 2.5×10^5 cells/well in 24-well assay
450 plates (Corning, 353047) in BMDM media. A duplicate plate was always plated for
451 total PI-positive cell number enumeration after overnight incubation using IncuCyte
452 ZOOM as described elsewhere. Bacterial cultures were prepared by picking a single
453 bacterial colony from TSA plates and grown in 10 mL tryptic soy broth (TSB) in a
454 shaking incubator overnight at 37 °C. After overnight incubation bacteria were

455 subcultured in fresh 10 mL of TSB at 37 °C until OD600 0.5 - 0.8, pelleted by
456 centrifugation, resuspended in 1:1000 poly-L-lysine (Sigma-Aldrich, P4707) in PBS
457 and incubated for 10 minutes at RT. Cell suspension was then centrifuged and the
458 pellet washed twice with PBS and once with the infection media [high glucose DMEM
459 (Genentech) + 10% FBS (VRW, custom manufactured for Genentech) + GlutaMAX
460 (Gibco, 30050-061)]. After the final wash the bacterial pellet was resuspended in the
461 infection media and OD600 was remeasured. To prepare multiplicity of infection
462 (MOI) of 5 in the infection media, total PI-positive object count per well was used for
463 accurate MOI calculations for every independent infection experiment. A cell
464 suspension containing lysine coated bacteria were added to the wells at MOI 5 in a
465 total volume of 250 µl/well and allowed to adhere by incubating for 30 minutes at 37
466 °C in a CO₂ incubator. After 30 minutes, bacterial suspension was aspirated and
467 replaced with 500 µl/well of fresh infection media supplemented with gentamicin at 50
468 µg/mL (Sigma-Aldrich, G1397). This was defined as the time-point T = 0 minutes.
469 Assay plates were subsequently incubated at 37 °C in a CO₂ incubator and used at
470 the indicated time-points for CFU enumeration.

471 **BMDM infections in 24-well plates with compounds.** For experiments with Erastin
472 (Sigma-Aldrich, E7781), day 5 BMDMs were plated at 2.5×10^5 cells/well in 24-well
473 assay plates (Corning, 353047) in BMDM media supplemented with Erastin at 4
474 µg/ml and incubated at 37 °C in a CO₂ incubator for 18 hours before infection. A
475 duplicate plate was also seeded and used for PI-positive object count per well
476 enumeration to ensure accurate MOI as described elsewhere. The bacterial culture
477 was prepared essentially as described elsewhere with the following modifications.
478 After the final wash with infection media the bacterial pellet was resuspended in the
479 infection media, OD600 was remeasured and bacterial suspension of MOI 10 was
480 prepared. A cell suspension containing lysine coated bacteria was mixed 1:1 with
481 infection media containing Erastin 8 µg/ml and added to the wells at MOI 5 in a total
482 volume of 250 µl/well and allowed to adhere by incubating for 30 minutes at 37 °C in
483 a CO₂ incubator. After 30 minutes, bacterial suspension was aspirated and replaced
484 with 500 µl/well of fresh infection media supplemented with gentamicin at 50 µg/mL
485 (Sigma-Aldrich, G1397) and Erastin at 4 µg/ml as indicated.

486 **BMDM infections in 15-cm dishes for TMT proteomics.** For large scale infections,
487 5-day differentiated BMDMs isolated from control *LysM-Cre*+ or *LysM-Cre*+
488 *Atg16L1*^{loxP/loxP} mice were plated at 10×10^6 cells per 15-cm non-TC treated dish

489 (Petri dish, VWR, 25384-326) in BMDM media. Bacterial suspension was prepared
490 essentially as described elsewhere with the following modifications. A suspension of
491 lysine coated bacteria in infection media were added to the dishes containing
492 BMDMs at MOI 5 in a volume of 15 ml/dish and allowed to adhere by incubating for
493 30 minutes at 37 °C in a CO₂ incubator. After 30 minutes, the medium was aspirated
494 and replaced with 50 ml/dish of fresh infection media supplemented with gentamicin
495 at 50 µg/mL (Sigma-Aldrich, G1397). This was defined as the time-point T = 0
496 minutes. Assay plates were subsequently placed at 37 °C in a CO₂ incubator and
497 samples collected after 30 - 45 minutes incubation ('early' infection time-point) or
498 after 3 - 3.5 hours incubation ('late' infection time-point). At the indicated time-points
499 a set of 10 dishes per genotype was used to prepare cell lysates for downstream
500 proteomic analysis. To prepare cell lysates, infection media was first aspirated and
501 cells washed once with PBS. Cells were then scrapped in the presence of Urea lysis
502 buffer (20mM HEPES pH 8.0, 9M Urea, 1mM sodium orthovanadate, 2.5 mM sodium
503 pyrophosphate, 1mM β-glycerolphosphate) and cell suspension stored at -80 °C until
504 further processing(Kirkpatrick et al., 2013).

505 **In vivo Shigella flexneri infection.** Mice were injected intravenously in the tail vein
506 with *Shigella flexneri* (M90T) bacterial culture that was prepared by picking a single
507 bacterial colony from TSA plates and grown in 10 mL tryptic soy broth (TSB) in a
508 shaking incubator overnight at 37 °C. After overnight incubation bacteria were sub-
509 cultured in fresh 10 mL of TSB at 37 °C until OD₆₀₀ 0.5 - 0.8, pelleted by
510 centrifugation, washed with PBS once, resuspended in PBS and OD₆₀₀ was
511 recounted. Each animal was injected with 100 µl of bacterial suspension in PBS
512 containing 2 x 10⁶ Colony Forming Units (CFUs) *S.flexneri* (M90T). Mice were
513 euthanized after 6 or 24 hours post infection to harvest spleen and liver for CFUs
514 enumeration and blood for cytokine profiling.

515 **Colony forming units (CFUs) assays.** To determine CFUs in infected BMDMs,
516 infection media was aspirated, cells were washed once with PBS and lysed by
517 adding 250 µl/well of 0.1 % Igepal CA-630 (Sigma-Aldrich, I8896) in PBS, incubated
518 for 5 minutes, resuspended and an aliquot of 200 µl was transferred to 96-well U-
519 bottom plate (Costar, 3799) for making two-step serial dilutions in 0.1 % Igepal CA-
520 630 in PBS. Subsequently, 5 µl of each serial dilution was plated on TSA plates in
521 triplicates, allowed to evaporate at RT after which the plate was placed in a 37 °C
522 incubator overnight. After overnight incubation, colonies from individual dilutions were

523 counted and used for determining CFUs per well. To determine CFUs in the liver,
524 mice were euthanized at the indicated time-points after infection and the livers were
525 surgically removed and placed in PBS on ice. Livers were processed in 5 ml of 0.1 %
526 Igepal CA-630 (Sigma-Aldrich, I8896) in PBS using the gentleMACS™ C Tubes
527 (Miltenyi Biotec, 130-096-334) in combination with the gentleMACS™ Octo
528 Dissociator (Miltenyi Biotec, 130-095-937) for the automated dissociation of tissues
529 using standard tissue dissociation programs (program sequence: m_liver_01_02;
530 m_liver_02_02, m_liver_01_02). Tissue suspensions were filtered through 100 µM
531 filters (CellTreat, 229485) and remaining liver tissue was additionally homogenized
532 using the rubber seal of the 5 ml syringe plunger. The resultant liver tissue
533 suspension was used for generating serial dilutions and plated on TSA plates for
534 CFUs enumeration as described elsewhere.

535 **IncuCyte assays.** For IncuCyte assays, BMDMs were plated at 2×10^4 cells/well in
536 flat-bottom 96-well (Corning, 353072) or at 2.5×10^5 cells/well in 24-well (Corning,
537 353047) assay plates. After overnight incubation at 37 °C in a CO₂ incubator, cells
538 were used for infection experiments or treatments with compounds or growth factors
539 as indicated. BMDM viability over time was assessed by supplementing assay media
540 [(high glucose DMEM (Genentech) + 10% FBS (VRW, custom manufactured for
541 Genentech) + GlutaMAX (Gibco, 30050-061) + Pen/Strep (Gibco, 15140-122)] with
542 propidium iodide (PI) dye for live-cell imaging at 1:1000 (Invitrogen, P3566), and then
543 measuring PI-positive cells per mm² using live cell imaging with IncuCyte ZOOM
544 (IncuCyte systems, Essen Biosciences) in a time-course experiment. Percent cell
545 death was calculated by dividing PI-positive cells per mm² with total plated cells per
546 mm². Total plated cells were enumerated from a duplicate plate seeded at the same
547 time as the assay plates. After overnight incubation, media in the duplicate plate was
548 exchanged to assay media containing 0.06 % NP-40 supplemented with 1:1000 PI,
549 and imaged at a single time-point using IncuCyte ZOOM after 10-minute incubation.

550 **GSH assays.** BMDMs were established as described and 5×10^6 of BMDMs were
551 pelleted by centrifugation, the pellet was lysed in mammalian lysis buffer (Abcam,
552 ab179835), incubated 10' at RT and centrifuged at top speed at 4 °C 15min.
553 Supernatant was transferred to a fresh tube and used for deproteinization following
554 manufacturer's instructions (Abcam, ab204708). The resultant supernatant was used
555 for determining reduced GSH, total GSH and oxidized GSSG was calculated as per
556 manufacturer's instructions (Abcam, ab138881).

557 **Fluorescence microscopy.** BMDMs grown on 96-well plates (Greiner Bio, 655090)
558 were treated with 10 μ M CellRox Green reagent for 30 minutes according to
559 manufacturer's protocol (Thermo Fisher Scientific, C10444), then fixed in 4 %
560 paraformaldehyde (PFA) solution in PBS (ChemCruz, SC281692) for 15 minutes at
561 RT. Nuclei were stained with NucBlue™ Live ReadyProbes™ Reagent (Thermo
562 Fisher Scientific, R37605) for 10 minutes in PBS. 3D confocal images corresponding
563 to 12 μ m thick z-stacks of 4 stitched fields of views were collected on a Nikon A1R
564 scanning confocal microscope using a Plan Apo NA 0.75 lens and x20
565 magnification. FITC and Hoechst 33342 signals were respectively imaged with the
566 488 nm and 405 nm laser lines. For each Z stack, images were combined into one
567 focused image using Nikon Elements Extended Depth of focus (EDF) module that
568 picks the focused regions from each frame and merges them together into a single
569 focused image. The focused EDF images from different conditions were then
570 analyzed with Bitplane Imaris software (version 9.2.0) using the cell segmentation
571 module and intensity quantification. To specifically determine the cytoplasmic
572 CellRox Green reagent intensity, the region corresponding to the Hoechst staining
573 was excluded and FITC channel threshold was applied across all samples per given
574 experiment. Mean cytosolic CellRox Green assay signal was then quantified per
575 each individual cell and presented in the graph.

576 **Transmission Electron Microscopy.** Samples were fixed in modified Karnovsky's
577 fixative (2% paraformaldehyde and 2.5% glutaraldehyde in 0.1M sodium cacodylate
578 buffer, pH7.2) and then post-fixed in freshly prepared 1% aqueous potassium
579 ferrocyanide- osmium tetroxide (EM Sciences, Hatfield, PA), for 2h followed by
580 overnight incubation in 0.5% Uranyl acetate at 4°C. The samples were then
581 dehydrated through ascending series of ethanol (50%, 70%, 90%, 100%) followed by
582 propylene oxide (each step was for 15 min) and embedded in Eponate 12 (Ted Pella,
583 Redding, CA). Ultrathin sections (80 nm) were cut with an Ultracut microtome (Leica),
584 stained with 0.2% lead citrate and examined in a JEOL JEM-1400 transmission
585 electron microscope (TEM) at 80kV. Digital images were captured with a GATAN
586 Ultrascan 1000 CCD camera.

587 **Tandem Mass Tag proteomics**

588 **Protein Precipitation.** Protein concentration in the lysates were quantified using the
589 Pierce micro-BCA assay (ThermoFisher Scientific, Waltham, MA). All protein from
590 the cell lysates was precipitated with a combination of

591 methanol/chloroform/water(Wessel and Flügge, 1984). In brief, X volume of lysate
592 was mixed with 4X volume of methanol followed by 2X volume of chloroform and 3X
593 volume of water. The protein pellets were washed a total of three times with 5X
594 volume of methanol. The protein pellets were air dried and resuspended in 8M urea,
595 100mM EPPS pH 7.0, 5mM DTT. Proteins were alkylated with 15 mM N-
596 ethylmaleimide (Sigma).

597 **LysC/Trypsin Digestion.** The protein in 8M urea was diluted to 4M with 100mM
598 EPPS, pH 8.0. 15 mg of protein/sample was digested at 25 °C for 12 hours with lysyl
599 endopeptidase (LysC, Wako Chemicals USA) at a 1:25; protein:protease ratio.
600 Following LysC digestion the peptides in 4M urea were diluted to 1M urea with
601 100mM EPPS, pH 8.0. The LysC peptides were digested with trypsin at 37 °C for 8
602 hours (Promega) at a 1:50; protein:protease ratio.

603 **Ubiquitin Remnant Peptide Enrichment (KGG peptides).** Prior to KGG peptide
604 enrichment, the tryptic peptides were acidified to 2% formic acid and desalted with 1
605 g tC18 Sep-Pak cartridges (Waters). The desalted peptides were dried by vacuum.
606 KGG peptide enrichment was performed with the PTMScan ubiquitin remnant motif
607 kit (Cell Signaling Technologies, Kit#5562) as per the manufacturers protocol. KGG
608 peptides eluted from the antibodies were dried by vacuum. The flow through peptides
609 from the KGG enrichment were saved for phosphopeptide and total protein analysis.

610 **TMT labelling of KGG Peptides.** Peptides were resuspended in 200mM EPPS, pH
611 8.0. 10 µL of TMT reagent at 20 µg/uL (ThermoFisher) was added to each sample.
612 Peptides were incubated with TMT reagent for 3 hours at 25 °C. TMT-labeled
613 peptides were quenched with hydroxylamine (0.5% final) and acidified with
614 trifluoroacetic acid (2% final). The samples were combined, desalted with 50 mg tC18
615 Sep-Paks, and dried by vacuum.

616 **Ubiquitin Remnant Peptide Fractionation.** TMT-labeled KGG peptides were
617 fractionated using the high pH reversed-phase peptide fractionation kit
618 (ThermoFisher). The dried KGG peptides were resuspended in 0.1% trifluoroacetic
619 acid and fractionated according to the manufacturers protocol into 6 fractions (17.5%,
620 20%, 22.5%, 25%, 30%, and 70% acetonitrile + 0.1% triethylamine). The KGG
621 peptide fractions were dried by vacuum, desalted with StageTips packed with
622 Empore C18 material (3M, Maplewood, MN.), and dried again by vacuum. KGG
623 peptides were reconstituted in 5% formic acid + 5% acetonitrile for LC-MS3 analysis.

624 **TMT labelling of KGG Flow Through Peptides.** The flow through peptides from the
625 KGG enrichment were labeled with TMT prior to phosphopeptide enrichment. The
626 flow through peptides were resuspended in 1X IAP buffer from the ubiquitin remnant
627 kit (from prior step). The pH of the resuspended peptides was adjusted by adding 1M
628 EPPS, pH 8.0 in a 3:1 ratio (peptide volume:1M EPPS volume; 250mM EPPS final).
629 2.1 mg of peptide from each sample was labeled with 2.4 mg of TMT reagent
630 resuspended in 60 μ L, 100% acetonitrile. The peptides were incubated with TMT
631 reagent for 3 hours at 25 °C. TMT-labeled peptides were quenched with
632 hydroxylamine (0.5% final) and acidified with trifluoroacetic acid (2% final). The
633 samples were combined, desalted with 1 g tC18 Sep-Paks, dried by vacuum.

634 **Phosphoserine, -threonine, -tyrosine Enrichment and Fractionation.**
635 Phosphotyrosine (pY) peptides were enriched using the Cell Signaling Technologies
636 pY-1000 antibody kit as per the manufacturers protocol (Cell Signaling Technologies,
637 Kit#8803). The flow through from the pY enrichment was desalted on a 1g tC18 Sep-
638 Pak cartridge (Waters Corporation, Milford, MA) and dried by centrifugal evaporation
639 and saved for phosphoserine and phosphothreonine (pST) analysis. pST
640 phosphopeptides were enriched using the Pierce Fe-NTA phospho-enrichment kit
641 (ThermoFisher). In brief, peptides were bound and washed as per manufacturers
642 protocol. Phosphopeptides were eluted from the Fe-NTA resin with 50mM HK_2PO_4
643 pH 10.5. Labelled phosphopeptides were subjected to orthogonal basic-pH reverse
644 phase fractionation on a 3x100 mm column packed with 1.9 μ m Poroshell C18
645 material (Agilent, Santa Clara, CA), utilizing a 45 min linear gradient from 8% buffer A
646 (5% acetonitrile in 10 mM ammonium bicarbonate, pH 8) to 30% buffer B (acetonitrile
647 in 10mM ammonium bicarbonate, pH 8) at a flow rate of 0.4 ml/min. Ninety-six
648 fractions were consolidated into 18 samples, acidified with formic acid and vacuum
649 dried. The samples were resuspended in 0.1% trifluoroacetic acid, desalted on
650 StageTips and vacuum dried. Peptides were reconstituted in 5% formic acid + 5%
651 acetonitrile for LC-MS3 analysis. The flow-through peptides from the pST enrichment
652 were saved for total protein analysis.

653 **Peptide Fractionation for Total Protein Analysis.** The flow-through from the pST
654 enrichment was dried by centrifugal evaporation. The dried peptides were
655 resuspended in 0.1% TFA. Approximately 250 μ g of peptide mix was subjected to
656 orthogonal basic-pH reverse phase fractionation on a 3x100 mm column packed with
657 1.9 μ m Poroshell C18 material (Agilent, Santa Clara, CA), utilizing a 45 min linear

gradient from 8% buffer A (5% acetonitrile in 10 mM ammonium bicarbonate, pH 8) to 35% buffer B (acetonitrile in 10mM ammonium bicarbonate, pH 8) at a flow rate of 0.4 ml/min. Ninety-six fractions were consolidated into 12 samples, acidified with formic acid and vacuum dried. The samples were resuspended in 5% formic acid, desalted on StageTips and vacuum dried. Peptides were reconstituted in 5% formic acid + 5% acetonitrile for LC-MS3 analysis.

Mass spectrometry analysis. All mass spectra were acquired on an Orbitrap Fusion Lumos coupled to an EASY nanoLC-1000 (or nanoLC-1200) (ThermoFisher) liquid chromatography system. Approximately 2 µg of peptides were loaded on a 75 µm capillary column packed in-house with Sepax GP-C18 resin (1.8 µm, 150 Å, Sepax Technologies) to a final length of 35 cm. Peptides for total protein analysis were separated using a 180-minute linear gradient from 8% to 23% acetonitrile in 0.1% formic acid. The mass spectrometer was operated in a data dependent mode. The scan sequence began with FTMS1 spectra (resolution = 120,000; mass range of 350-1400 *m/z*; max injection time of 50 ms; AGC target of 1e6; dynamic exclusion for 60 seconds with a +/- 10 ppm window). The ten most intense precursor ions were selected for ITMS2 analysis via collisional-induced dissociation (CID) in the ion trap (normalized collision energy (NCE) = 35; max injection time = 100ms; isolation window of 0.7 Da; AGC target of 2e4). Following ITMS2 acquisition, a synchronous-precursor-selection (SPS) MS3 spectrum was acquired by selecting and isolating up to 10 MS2 product ions for additional fragmentation via high energy collisional-induced dissociation (HCD) with analysis in the Orbitrap (NCE = 55; resolution = 50,000; max injection time = 110 ms; AGC target of 1.5e5; isolation window at 1.2 Da for +2 *m/z*, 1.0 Da for +3 *m/z* or 0.8 Da for +4 to +6 *m/z*).

pY peptides were separated using a 180-minute linear gradient from 7% to 26% acetonitrile in 0.1% formic acid. The mass spectrometer was operated in a data dependent mode. The scan sequence began with FTMS1 spectra (resolution = 120,000; mass range of 350-1400 *m/z*; max injection time of 50 ms; AGC target of 1e6; dynamic exclusion for 75 seconds with a +/- 10 ppm window). The ten most intense precursor ions were selected for FTMS2 analysis via collisional-induced dissociation (CID) in the ion trap (normalized collision energy (NCE) = 35; max injection time = 150ms; isolation window of 0.7 Da; AGC target of 3e4; *m/z* = 2-6; Orbitrap resolution = 15k). Following FTMS2 acquisition, a synchronous-precursor-selection (SPS) MS3 method was enabled to select five MS2 product ions for high

692 energy collisional-induced dissociation (HCD) with analysis in the Orbitrap (NCE =
693 55; resolution = 50,000; max injection time = 300 ms; AGC target of 1e5; isolation
694 window at 1.2 Da).

695 pST peptides were separated using a 120-minute linear gradient from 6% to
696 26% acetonitrile in 0.1% formic acid. The mass spectrometer was operated in a data
697 dependent mode. The scan sequence began with FTMS1 spectra (resolution =
698 120,000; mass range of 350-1400 *m/z*; max injection time of 50 ms; AGC target of
699 1e6; dynamic exclusion for 60 seconds with a +/- 10 ppm window). The ten most
700 intense precursor ions were selected for ITMS2 analysis via collisional-induced
701 dissociation (CID) in the ion trap (normalized collision energy (NCE) = 35; max
702 injection time = 200ms; isolation window of 0.7 Da; AGC target of 2e4). Following
703 MS2 acquisition, a synchronous-precursor-selection (SPS) MS3 method was enabled
704 to select five MS2 product ions for high energy collisional-induced dissociation (HCD)
705 with analysis in the Orbitrap (NCE = 55; resolution = 50,000; max injection time = 300
706 ms; AGC target of 1e5; isolation window at 1.2 Da for +2 *m/z*, 1.0 Da for +3 *m/z* or
707 0.8 Da for +4 to +6 *m/z*).

708 KGG peptides were separated using a 180-minute linear gradient from 7% to
709 24% acetonitrile in 0.1% formic acid. The mass spectrometer was operated in a data
710 dependent mode. The scan sequence began with FTMS1 spectra (resolution =
711 120,000; mass range of 350-1400 *m/z*; max injection time of 50 ms; AGC target of
712 1e6; dynamic exclusion for 75 seconds with a +/- 10 ppm window). The ten most
713 intense precursor ions were selected for FTMS2 analysis via collisional-induced
714 dissociation (CID) in the ion trap (normalized collision energy (NCE) = 35; max
715 injection time = 100ms; isolation window of 0.7 Da; AGC target of 5e4; *m/z* 3-6,
716 Orbitrap resolution set to 15k). Following MS2 acquisition, a synchronous-precursor-
717 selection (SPS) MS3 method was enabled to select 10 MS2 product ions for high
718 energy collisional-induced dissociation (HCD) with analysis in the Orbitrap (NCE =
719 55; resolution = 50,000; max injection time = 500 ms; AGC target of 1e5; isolation
720 window at 1.0 Da for +3 *m/z* or 0.8 Da for +4 to +6 *m/z*).

721 MS/MS spectra for the global proteome, serine/threonine phosphorylated,
722 tyrosine phosphorylated, and ubiquitylated data sets were searched using the Mascot
723 search algorithm (Matrix Sciences) against a concatenated target-decoy database
724 comprised of the UniProt mouse and *Shigella flexneri* protein sequences (version
725 2017_08), known contaminants and the reversed versions of each sequence. For all

726 datasets a 50 ppm precursor ion mass tolerance was selected with tryptic specificity
727 up to two missed cleavages. For the global proteome and serine/ threonine
728 phosphorylated datasets a 0.8 Da fragment ion tolerance was selected. While for the
729 tyrosine phosphorylated and KGG (ubiquitin) datasets a 0.02 Da fragment ion
730 tolerance was selected. The global proteome and phosphorylated datasets used a
731 fixed modification of N-ethylmaleimide on cysteine residues (+125.0477) as well as
732 TMT 11-plex on Lysine and the peptide N-term (+229.1629). The ubiquitylated data
733 set used a fixed modification of N-ethylmaleimide on cysteine residues (+125.0477)
734 as well as TMT 11-plex on the peptide N-term (+229.1629). For variable
735 modifications the global proteome dataset used methionine oxidation (+15.9949) as
736 well as TMT 11-plex on tyrosine (+229.1629). The phosphorylated dataset used the
737 same variable modifications as the global proteome dataset plus phosphorylation on
738 serine, threonine, and tyrosine (+79.9663). Finally, the ubiquitylated dataset used
739 methionine oxidation (+15.9949), TMT 11 plex on tyrosine and lysine (+229.1629), as
740 well as TMT 11 Plex + ubiquitylation on lysine (343.2059). PSMs were filtered to a
741 1% peptide FDR at the run level using linear discriminant analysis (LDA) (Kirkpatrick
742 et al., 2013). PSM data within each plex and dataset (global proteome,
743 phosphorylation, and ubiquitylation) was aggregated and these results were
744 subsequently filtered to 2% protein FDR. For PSMs passing the peptide and protein
745 FDR filters within the phosphorylated and ubiquitylated datasets, phosphorylation
746 and ubiquitylation site localization was assessed using a modified version of the
747 AScore algorithm(Beausoleil et al., 2006) and reassigned accordingly. Finally,
748 reporter ion intensity values were determined for each dataset and plex using the
749 Mojave algorithm(Zhuang et al., 2013) with an isolation width of 0.7.

750 **Quantification and statistical testing of global proteomics and**
751 **phosphoproteomic data.** Quantification and statistical testing of global proteomics
752 data were performed by MSstatsTMT v1.2.7, an open-source R/Bioconductor
753 package(Huang et al., 2020; Tsai et al., 2020). MSstatsTMT was used to create
754 quantification reports and statistical testing reports using the Peptide Spectrum
755 Matches (PSM) as described above. First, PSMs were filtered out if they were (1)
756 from decoy proteins; (2) from peptides with length less than 7; (3) with isolation
757 specificity less than 70%; (4) with reporter ion intensity less than 2^8 noise estimate;
758 (5) from peptides shared by more than one protein; (6) with summed reporter ion
759 intensity (across all eleven channels) lower than 30,000; (7) with missing values in

more than nine channels. In the case of redundant PSMs (i.e., multiple PSMs in one MS run corresponding to the same peptide ion), only the single PSM with the least missing values or highest isolation specificity or highest maximal reporter ion intensity was retained for subsequent analysis. Multiple fractions from the same TMT mixture were combined in MSstatsTMT. In particular, if the same peptide ion was identified in multiple fractions, only the single fraction with the highest mean or maximal reporter ion intensity was kept. Next, MSstatsTMT generated a normalized quantification report across all the samples at the protein level from the processed PSM report. Global median normalization, which equalized the median of the reporter ion intensities across all the channels and TMT mixtures, was carried out to reduce the systematic bias between channels. The normalized reporter ion intensities of all the peptide ions mapped to a protein were summarized into a single protein level intensity in each channel and TMT mixture. For each protein, additional local normalization on the summaries was performed to reduce the systematic bias between different TMT mixtures. For the local normalization, we created an artifact reference channel by averaging over all the channels except 131C for each protein and TMT mixture. The channel 131C was removed in order to make each mixture have the same number of samples from each condition. The normalized quantification report at the protein level is available in Supplementary Table 6. As a final step, the differential abundance analysis between conditions was performed in MSstatsTMT based on a linear mixed-effects model per protein. The inference procedure was adjusted by applying an empirical Bayes shrinkage. The table with the statistical testing results for all the proteins is available as in Supplementary Table 7. Quantification and statistical testing for phospho- and KGG (Ub) site data were performed by the same procedure as for global proteomics data with some modifications. First, PSMs from non-modified peptides were filtered out from the PSM report and the remaining preprocessing analyses were the same as above. Second, custom PTM site identifiers were created for each PSM by identifying the modified residue index in the reference proteome that was used to search the MS/MS spectra. Finally, all steps for quantification and differential abundance analysis were performed at the PTM site level, rather than the protein level (Supplementary Tables 8 and 9). The relative abundance of TMT reporter ion abundances in bar graphs throughout the paper stems from MSstats modeling and sums up to 1.0 for each Plex. Thus, the sum of all signal shown sums to 1.0 or 2.0 depending on whether the

794 feature was quantified in one or both plexes. For the consolidated heatmaps showing
795 proteome level changes immediately adjacent to any identified PTMs, the
796 ComplexHeatmap R package was used.

797 **Gene set enrichment analysis.** Gene set enrichment analysis was performed using
798 MsigDB(Liberzon et al., 2015; Subramanian et al., 2005). Global proteome data were
799 filtered to include features with an absolute value log2fc values of greater than 1 as
800 well as p values of less than 0.05. Subsequently the data were filtered to require that
801 every protein must be found in both multiplexed experiments. UniProt identifiers were
802 transformed to gene symbols and fed into GSEA for an enrichment analysis against
803 MsigDB's hallmark gene sets. Gene set enrichment results were filtered to 5% FDR.

804 **Overview Heatmaps/Clustering.** For the overview heatmaps showing PTM and
805 global proteome datasets side by side, clustering was performed as follows. First,
806 protein quantification results from MSstatsTMT for the PTM and global proteome
807 datasets were merged with the phospho-proteome and KGG datasets, respectively.
808 For each of the two combined datasets, the pheatmap R package was used to
809 cluster the protein model results into 16 row wise clusters using the clustering
810 method 'ward.D'. The columns of the dataset were kept static and not clustered.

811 **Statistical analysis.** Pairwise statistical analyses were performed using an unpaired
812 t-test using two-stage step-up method of Benjamini, Krieger and Yekutieli and false
813 discovery rate of 1% to determine if the values in two sets of data differ. Multiple-
814 comparison corrections were made using the Sidak method with family-wise
815 significance and confidence level of 0.05. Analysis of *in vivo* infection data was done
816 using unpaired two-tailed t-test after outliers were removed using ROUT method (Q =
817 1 %). Analysis of kinetic (time) with Erastin was performed using two-way ANOVA
818 followed by multiple comparison testing. Line graphs and associated data points
819 represent means of data; error bars represent standard deviation from mean.
820 GraphPad Prism 8 software was used for data analysis and representation. P-values:
821 * <0.05 , ** <0.01 , *** <0.001 , **** <0.0001 . For proteomics data, differential abundance
822 analysis between conditions and p-values were determined based on a linear mixed-
823 effects model per protein (global proteome data) or per PTM site (Phosphorylation,
824 Ubiquitin-KGG data) using MSstatsTMT software package.

825 **Data availability.** Mass spectrometry raw files have been uploaded to the UCSD
826 MassIVE repository and are available:

827 (<https://massive.ucsd.edu/ProteoSAFe/dataset.jsp?accession=MSV000085565>;
828 Password= shigella).

829 **Software Availability.** Raw files were converted to mzXML using ReadW (v 4.3.1)
830 available
831 through <https://sourceforge.net/projects/sashimi/files/ReAdW%20%28Xcalibur%20co>
832 [nverter%29/](#). Spectra were searched using Mascot (v 2.4.1) licensed from Matrix
833 Sciences. Search results were filtered using the LDA function in the MASS Package
834 in R as described in Huttlin et al. Cell 143, 1147-1189 (2010). Mojave is an in-house
835 tool developed to report TMT reporter ion intensity values and is available upon
836 request. MSstatsTMT (v 1.2.7) is a freely available open-source R/Bioconductor
837 package to detect differentially abundant proteins in TMT experiments. It can be
838 installed
839 through <https://www.bioconductor.org/packages/release/bioc/html/MSstatsTMT.html>.
840 Gene set enrichment was performed using the GSEA/MSigDB web
841 portal <https://www.gsea-msigdb.org/gsea/msigdb/annotate.jsp>. Heatmaps were
842 generated using the pheatmap (v1.0.12) (<https://cran.r-project.org/web/packages/pheatmap/index.html>) or ComplexHeatmap (v 2.4.2)
843 (<https://bioconductor.org/packages/release/bioc/html/ComplexHeatmap.html>) R
844 packages.
845

846 **References**

- 847 Ashida, H., Mimuro, H., and Sasakawa, C. (2015). Shigella Manipulates Host Immune
848 Responses by Delivering Effector Proteins with Specific Roles. *Front. Immunol.* **6**.
- 849 Bauckman, K.A., Owusu-Boaitey, N., and Mysorekar, I.U. (2015). Selective autophagy:
850 Xenophagy. *Methods* **75**, 120–127.
- 851 Beausoleil, S.A., Villén, J., Gerber, S.A., Rush, J., and Gygi, S.P. (2006). A probability-based
852 approach for high-throughput protein phosphorylation analysis and site localization. *Nat.*
853 *Biotechnol.* **24**, 1285–1292.
- 854 Bingol, B., Tea, J.S., Phu, L., Reichelt, M., Bakalarski, C.E., Song, Q., Foreman, O., Kirkpatrick,
855 D.S., and Sheng, M. (2014). The mitochondrial deubiquitinase USP30 opposes parkin-
856 mediated mitophagy. *Nature* **510**, 370–375.
- 857 Birmingham, C.L., Smith, A.C., Bakowski, M.A., Yoshimori, T., and Brumell, J.H. (2006).
858 Autophagy Controls Salmonella Infection in Response to Damage to the Salmonella-
859 containing Vacuole. *J. Biol. Chem.* **281**, 11374–11383.
- 860 Cadwell, K., Patel, K.K., Maloney, N.S., Liu, T.-C., Ng, A.C.Y., Storer, C.E., Head, R.D., Xavier, R.,
861 Stappenbeck, T.S., and Virgin, H.W. (2010). Virus-Plus-Susceptibility Gene Interaction
862 Determines Crohn's Disease Gene Atg16L1 Phenotypes in Intestine. *Cell* **141**, 1135–1145.
- 863 Campbell-Valois, F.-X., Sachse, M., Sansonetti, P.J., and Parsot, C. (2015). Escape of Actively
864 Secreting *Shigella flexneri* from ATG8/LC3-Positive Vacuoles Formed during Cell-To-Cell
865 Spread Is Facilitated by lcsB and VirA. *MBio* **6**.
- 866 Choi, S.-W., Park, H.-H., Kim, S., Chung, J.M., Noh, H.-J., Kim, S.K., Song, H.K., Lee, C.-W.,
867 Morgan, M.J., Kang, H.C., et al. (2018). PELI1 Selectively Targets Kinase-Active RIP3 for
868 Ubiquitylation-Dependent Proteasomal Degradation. *Mol. Cell* **70**, 920–935.e7.
- 869 Choy, A., Dancourt, J., Mugo, B., O'Connor, T.J., Isberg, R.R., Melia, T.J., and Roy, C.R. (2012).
870 The Legionella Effector RavZ Inhibits Host Autophagy Through Irreversible Atg8
871 Deconjugation. *Science* **338**, 1072–1076.
- 872 Conrad, M., and Sato, H. (2012). The oxidative stress-inducible cystine/glutamate antiporter,
873 system x_c⁻: cystine supplier and beyond. *Amino Acids* **42**, 231–246.
- 874 Cunha, L.D., Yang, M., Carter, R., Guy, C., Harris, L., Crawford, J.C., Quarato, G., Boada-
875 Romero, E., Kalkavan, H., Johnson, M.D.L., et al. (2018). LC3-Associated Phagocytosis in
876 Myeloid Cells Promotes Tumor Immune Tolerance. *Cell* **175**, 429–441.e16.
- 877 DeVorkin, L., Pavey, N., Carleton, G., Comber, A., Ho, C., Lim, J., McNamara, E., Huang, H.,
878 Kim, P., Zacharias, L.G., et al. (2019). Autophagy Regulation of Metabolism Is Required for
879 CD8+ T Cell Anti-tumor Immunity. *Cell Rep.* **27**, 502–513.e5.
- 880 Dixon, S.J., Lemberg, K.M., Lamprecht, M.R., Skouta, R., Zaitsev, E.M., Gleason, C.E., Patel,
881 D.N., Bauer, A.J., Cantley, A.M., Yang, W.S., et al. (2012). Ferroptosis: an iron-dependent
882 form of nonapoptotic cell death. *Cell* **149**, 1060–1072.

- 884 Dong, N., Zhu, Y., Lu, Q., Hu, L., Zheng, Y., and Shao, F. (2012). Structurally Distinct Bacterial
885 TBC-like GAPs Link Arf GTPase to Rab1 Inactivation to Counteract Host Defenses. *Cell* **150**,
886 1029–1041.
- 887 Fujita, N., Morita, E., Itoh, T., Tanaka, A., Nakaoka, M., Osada, Y., Umemoto, T., Saitoh, T.,
888 Nakatogawa, H., Kobayashi, S., et al. (2013). Recruitment of the autophagic machinery to
889 endosomes during infection is mediated by ubiquitin. *J. Cell Biol.* **203**, 115–128.
- 890 Gao, L., Cope, H., Grant, S., Ma, A., Ley, S.C., and Harhaj, E.W. (2011). ABIN1 Protein
891 Cooperates with TAX1BP1 and A20 Proteins to Inhibit Antiviral Signaling. *J. Biol. Chem.* **286**,
892 36592–36602.
- 893 Hampe, J., Franke, A., Rosenstiel, P., Till, A., Teuber, M., Huse, K., Albrecht, M., Mayr, G.,
894 Vega, F.M.D.L., Briggs, J., et al. (2007). A genome-wide association scan of nonsynonymous
895 SNPs identifies a susceptibility variant for Crohn disease in ATG16L1. *Nat. Genet.* **39**, 207–
896 211.
- 897 Huang, J., and Brumell, J.H. (2014). Bacteria-autophagy interplay: a battle for survival. *Nat. Rev. Microbiol.* **12**, 101–114.
- 899 Huang, T., Choi, M., Hao, S., and Vitek, O. (2020). MSstatsTMT: Protein Significance Analysis
900 in shotgun mass spectrometry-based proteomic experiments with tandem mass tag (TMT)
901 labeling (Bioconductor version: Release (3.11)).
- 902 Hubbard-Lucey, V.M., Shono, Y., Maurer, K., West, M.L., Singer, N.V., Ziegler, C.G.K.,
903 Lezcano, C., Motta, A.C.F., Schmid, K., Levi, S.M., et al. (2014). Autophagy Gene Atg16l1
904 Prevents Lethal T Cell Alloreactivity Mediated by Dendritic Cells. *Immunity* **41**, 579–591.
- 905 Kirkpatrick, D.S., Bustos, D.J., Dogan, T., Chan, J., Phu, L., Young, A., Friedman, L.S., Belvin,
906 M., Song, Q., Bakalarski, C.E., et al. (2013). Phosphoproteomic characterization of DNA
907 damage response in melanoma cells following MEK/PI3K dual inhibition. *Proc. Natl. Acad.
908 Sci.* **110**, 19426–19431.
- 909 Koch, A., Yoon, Y., Bonekamp, N.A., McNiven, M.A., and Schrader, M. (2005). A role for Fis1
910 in both mitochondrial and peroxisomal fission in mammalian cells. *Mol. Biol. Cell* **16**, 5077–
911 5086.
- 912 Lapek, J.D., Greninger, P., Morris, R., Amzallag, A., Pruteanu-Malinici, I., Benes, C.H., and
913 Haas, W. (2017). Detection of dysregulated protein-association networks by high-throughput
914 proteomics predicts cancer vulnerabilities. *Nat. Biotechnol.* **35**, 983–989.
- 915 Lassen, K.G., Kuballa, P., Conway, K.L., Patel, K.K., Becker, C.E., Peloquin, J.M., Villablanca,
916 E.J., Norman, J.M., Liu, T.-C., Heath, R.J., et al. (2014). Atg16L1 T300A variant decreases
917 selective autophagy resulting in altered cytokine signaling and decreased antibacterial
918 defense. *Proc. Natl. Acad. Sci.* **111**, 7741–7746.
- 919 Lee, S., Tumolo, J.M., Ehlinger, A.C., Jernigan, K.K., Qualls-Histed, S.J., Hsu, P.-C., McDonald,
920 W.H., Chazin, W.J., and MacGurn, J.A. (2017). Ubiquitin turnover and endocytic trafficking in
921 yeast are regulated by Ser57 phosphorylation of ubiquitin. *ELife* **6**, e29176.

- 922 Li, P., Jiang, W., Yu, Q., Liu, W., Zhou, P., Li, J., Xu, J., Xu, B., Wang, F., and Shao, F. (2017).
923 Ubiquitination and degradation of GBPs by a *Shigella* effector to suppress host defence.
924 *Nature* 551, 378–383.
- 925 Liberzon, A., Birger, C., Thorvaldsdóttir, H., Ghandi, M., Mesirov, J.P., and Tamayo, P. (2015).
926 The Molecular Signatures Database (MSigDB) hallmark gene set collection. *Cell Syst.* 1, 417–
927 425.
- 928 Lim, J., Park, H., Heisler, J., Maculins, T., Roose-Girma, M., Xu, M., Mckenzie, B., van
929 Lookeren Campagne, M., Newton, K., and Murthy, A. (2019). Autophagy regulates
930 inflammatory programmed cell death via turnover of RHIM-domain proteins. *ELife* 8.
- 931 Liu, W., Zhou, Y., Peng, T., Zhou, P., Ding, X., Li, Z., Zhong, H., Xu, Y., Chen, S., Hang, H.C., et
932 al. (2018). N ε -fatty acylation of multiple membrane-associated proteins by *Shigella* IcsB
933 effector to modulate host function. *Nat. Microbiol.* 3, 996–1009.
- 934 Maloy, K.J., and Powrie, F. (2011). Intestinal homeostasis and its breakdown in inflammatory
935 bowel disease. *Nature* 474, 298–306.
- 936 Marchiando, A.M., Ramanan, D., Ding, Y., Gomez, L.E., Hubbard-Lucey, V.M., Maurer, K.,
937 Wang, C., Ziel, J.W., van Rooijen, N., Nuñez, G., et al. (2013). A deficiency in the autophagy
938 gene Atg16L1 enhances resistance to enteric bacterial infection. *Cell Host Microbe* 14, 216–
939 224.
- 940 Martin, P.K., Marchiando, A., Xu, R., Rudensky, E., Yeung, F., Schuster, S.L., Kernbauer, E.,
941 and Cadwell, K. (2018). Autophagy proteins suppress protective type I interferon signalling in
942 response to the murine gut microbiota. *Nat. Microbiol.* 3, 1131–1141.
- 943 Matsuzawa-Ishimoto, Y., Shono, Y., Gomez, L.E., Hubbard-Lucey, V.M., Cammer, M., Neil, J.,
944 Dewan, M.Z., Lieberman, S.R., Lazrak, A., Marinis, J.M., et al. (2017). Autophagy protein
945 ATG16L1 prevents necroptosis in the intestinal epithelium. *J. Exp. Med.* 214, 3687–3705.
- 946 McAlister, G.C., Nusinow, D.P., Jedrychowski, M.P., Wühr, M., Huttlin, E.L., Erickson, B.K.,
947 Rad, R., Haas, W., and Gygi, S.P. (2014). MultiNotch MS3 enables accurate, sensitive, and
948 multiplexed detection of differential expression across cancer cell line proteomes. *Anal. Chem.* 86, 7150–7158.
- 950 Mostowy, S., Bonazzi, M., Hamon, M.A., Tham, T.N., Mallet, A., Lelek, M., Gouin, E.,
951 Demangel, C., Brosch, R., Zimmer, C., et al. (2010). Entrapment of intracytosolic bacteria by
952 septin cage-like structures. *Cell Host Microbe* 8, 433–444.
- 953 Murthy, A., Li, Y., Peng, I., Reichelt, M., Katakam, A.K., Noubade, R., Roose-Girma, M.,
954 DeVoss, J., Diehl, L., Graham, R.R., et al. (2014). A Crohn's disease variant in Atg16l1
955 enhances its degradation by caspase 3. *Nature* 506, 456–462.
- 956 Ogawa, M., Yoshimori, T., Suzuki, T., Sagara, H., Mizushima, N., and Sasakawa, C. (2005).
957 Escape of Intracellular *Shigella* from Autophagy. *Science* 307, 727–731.
- 958 Orvedahl, A., McAllaster, M.R., Sansone, A., Dunlap, B.F., Desai, C., Wang, Y.-T., Balce, D.R.,
959 Luke, C.J., Lee, S., Orchard, R.C., et al. (2019). Autophagy genes in myeloid cells counteract

- 960 IFNy-induced TNF-mediated cell death and fatal TNF-induced shock. Proc. Natl. Acad. Sci. U.
961 S. A. 116, 16497–16506.
- 962 Parvatiyar, K., Barber, G.N., and Harhaj, E.W. (2010). TAX1BP1 and A20 Inhibit Antiviral
963 Signaling by Targeting TBK1-IKK α Kinases. J. Biol. Chem. 285, 14999–15009.
- 964 Peng, J., Schwartz, D., Elias, J.E., Thoreen, C.C., Cheng, D., Marsischky, G., Roelofs, J., Finley,
965 D., and Gygi, S.P. (2003). A proteomics approach to understanding protein ubiquitination.
966 Nat. Biotechnol. 21, 921–926.
- 967 Rioux, J.D., Xavier, R.J., Taylor, K.D., Silverberg, M.S., Goyette, P., Huett, A., Green, T.,
968 Kuballa, P., Barmada, M.M., Datta, L.W., et al. (2007). Genome-wide association study
969 identifies new susceptibility loci for Crohn disease and implicates autophagy in disease
970 pathogenesis. Nat. Genet. 39, 596–604.
- 971 Rose, C.M., Isasa, M., Ordureau, A., Prado, M.A., Beausoleil, S.A., Jedrychowski, M.P., Finley,
972 D.J., Harper, J.W., and Gygi, S.P. (2016). Highly Multiplexed Quantitative Mass Spectrometry
973 Analysis of Ubiquitylomes. Cell Syst. 3, 395–403.e4.
- 974 Saitoh, T., Fujita, N., Jang, M.H., Uematsu, S., Yang, B.-G., Satoh, T., Omori, H., Noda, T.,
975 Yamamoto, N., Komatsu, M., et al. (2008). Loss of the autophagy protein Atg16L1 enhances
976 endotoxin-induced IL-1 β production. Nature 456, 264–268.
- 977 Samie, M., Lim, J., Verschueren, E., Baughman, J.M., Peng, I., Wong, A., Kwon, Y.,
978 Senbabaoglu, Y., Hackney, J.A., Keir, M., et al. (2018). Selective autophagy of the adaptor
979 TRIF regulates innate inflammatory signaling. Nat. Immunol. 19, 246–254.
- 980 Sato, H., Tamba, M., Ishii, T., and Bannai, S. (1999). Cloning and Expression of a Plasma
981 Membrane Cystine/Glutamate Exchange Transporter Composed of Two Distinct Proteins. J.
982 Biol. Chem. 274, 11455–11458.
- 983 Shembade, N., Pujari, R., Harhaj, N.S., Abbott, D.W., and Harhaj, E.W. (2011). The kinase
984 IKK α inhibits activation of the transcription factor NF- κ B by phosphorylating the regulatory
985 molecule TAX1BP1. Nat. Immunol. 12, 834–843.
- 986 Sidik, S., Kottwitz, H., Benjamin, J., Ryu, J., Jarrar, A., Garduno, R., and Rohde, J.R. (2014). A
987 Shigella flexneri Virulence Plasmid Encoded Factor Controls Production of Outer Membrane
988 Vesicles. G3 Genes Genom. 4, 2493–2503.
- 989 Stoltz, A., Ernst, A., and Dikic, I. (2014). Cargo recognition and trafficking in selective
990 autophagy. Nat. Cell Biol. 16, 495–501.
- 991 Subramanian, A., Tamayo, P., Mootha, V.K., Mukherjee, S., Ebert, B.L., Gillette, M.A.,
992 Paulovich, A., Pomeroy, S.L., Golub, T.R., Lander, E.S., et al. (2005). Gene set enrichment
993 analysis: a knowledge-based approach for interpreting genome-wide expression profiles.
994 Proc. Natl. Acad. Sci. U. S. A. 102, 15545–15550.
- 995 Tal, M.C., Sasai, M., Lee, H.K., Yordy, B., Shadel, G.S., and Iwasaki, A. (2009). Absence of
996 autophagy results in reactive oxygen species-dependent amplification of RLR signaling. Proc.
997 Natl. Acad. Sci. 106, 2770–2775.

- 998 Thurston, T.L.M., Wandel, M.P., Muhlinen, N. von, Foeglein, Á., and Randow, F. (2012).
999 Galectin 8 targets damaged vesicles for autophagy to defend cells against bacterial invasion.
1000 *Nature* 482, 414–418.
- 1001 Ting, L., Rad, R., Gygi, S.P., and Haas, W. (2011). MS3 eliminates ratio distortion in isobaric
1002 multiplexed quantitative proteomics. *Nat. Methods* 8, 937–940.
- 1003 Tokunaga, F., Sakata, S., Saeki, Y., Satomi, Y., Kirisako, T., Kamei, K., Nakagawa, T., Kato, M.,
1004 Murata, S., Yamaoka, S., et al. (2009). Involvement of linear polyubiquitylation of NEMO in
1005 NF-κappaB activation. *Nat. Cell Biol.* 11, 123–132.
- 1006 Tsai, T.-H., Choi, M., Banfai, B., Liu, Y., MacLean, B., Dunkley, T., and Vitek, O. (2020).
1007 Selection of features with consistent profiles improves relative protein quantification in
1008 mass spectrometry experiments. *Mol. Cell. Proteomics MCP*.
- 1009 Wandel, M.P., Pathe, C., Werner, E.I., Ellison, C.J., Boyle, K.B., von der Malsburg, A., Rohde,
1010 J., and Randow, F. (2017). GBPs Inhibit Motility of *Shigella flexneri* but Are Targeted for
1011 Degradation by the Bacterial Ubiquitin Ligase IpaH9.8. *Cell Host Microbe* 22, 507-518.e5.
- 1012 Wang, C., Bauckman, K.A., Ross, A.S.B., Symington, J.W., Ligon, M.M., Scholtes, G., Kumar,
1013 A., Chang, H.-W., Twentyman, J., Fashemi, B.E., et al. (2019). A non-canonical autophagy-
1014 dependent role of the ATG16L1T300A variant in urothelial vesicular trafficking and
1015 uropathogenic *Escherichia coli* persistence. *Autophagy* 15, 527–542.
- 1016 Wang, W., Hu, Y., Wang, X., Wang, Q., and Deng, H. (2018). ROS-Mediated 15-
1017 Hydroxyprostaglandin Dehydrogenase Degradation via Cysteine Oxidation Promotes NAD+-
1018 Mediated Epithelial-Mesenchymal Transition. *Cell Chem. Biol.* 25, 255-261.e4.
- 1019 Wang, Y.-T., Zaitsev, K., Lu, Q., Li, S., Schaiff, W.T., Kim, K.-W., Droit, L., Wilen, C.B., Desai, C.,
1020 Balce, D.R., et al. (2020). Select autophagy genes maintain quiescence of tissue-resident
1021 macrophages and increase susceptibility to *Listeria monocytogenes*. *Nat. Microbiol.* 5, 272–
1022 281.
- 1023 Wessel, D., and Flügge, U.I. (1984). A method for the quantitative recovery of protein in
1024 dilute solution in the presence of detergents and lipids. *Anal. Biochem.* 138, 141–143.
- 1025 Xu, D., Li, X., Shao, F., Lv, G., Lv, H., Lee, J.-H., Qian, X., Wang, Z., Xia, Y., Du, L., et al. (2019a).
1026 The protein kinase activity of fructokinase A specifies the antioxidant responses of tumor
1027 cells by phosphorylating p62. *Sci. Adv.* 5, eaav4570.
- 1028 Xu, Y., Zhou, P., Cheng, S., Lu, Q., Nowak, K., Hopp, A.-K., Li, L., Shi, X., Zhou, Z., Gao, W., et
1029 al. (2019b). A Bacterial Effector Reveals the V-ATPase-ATG16L1 Axis that Initiates
1030 Xenophagy. *Cell* 178, 552-566.e20.
- 1031 Zhang, Q., Wu, J., Wu, R., Ma, J., Du, G., Jiao, R., Tian, Y., Zheng, Z., and Yuan, Z. (2012). DJ-1
1032 promotes the proteasomal degradation of Fis1: implications of DJ-1 in neuronal protection.
1033 *Biochem. J.* 447, 261–269.

1034 Zhuang, G., Yu, K., Jiang, Z., Chung, A., Yao, J., Ha, C., Toy, K., Soriano, R., Haley, B.,
1035 Blackwood, E., et al. (2013). Phosphoproteomic analysis implicates the mTORC2-FoxO1 axis
1036 in VEGF signaling and feedback activation of receptor tyrosine kinases. *Sci. Signal.* 6, ra25.

1037

1038 **Funding**

1039 This work was funded in parts by a fellowship awarded to T.M. by the AXA
1040 Research fund (16-AXA-PDOC-078) and the Genentech Visiting Scientist Program.

1041

1042 **Acknowledgements**

1043 We thank Avinashnarayan Venkatanarayan and the laboratory of Eric Brown
1044 at Genentech for technical assistance.

1045

1046 **Author contributions**

1047 T.M., I.D., D.S.K. and A.M. designed the conceptual framework of the study
1048 and experiments. T.M. designed and performed large-scale proteomic experiments
1049 with assistance from J.L. and guidance from I.D., D.S.K. and A.M. TMT data
1050 acquisition and initial data analysis performed by R.C.K., B.K.E., T.H., M.C., T-H. T.
1051 and O.V. TMT data analysis and representation performed by T.H., E.V. and D.S.K.
1052 with input from T.M. and A.M. Electron microscopy performed by A.K.K. and M.R.
1053 CellRox microscopy experiments performed by T.M., P.C. and C.C. *In vitro* BMDM
1054 infection assays performed by T.M. *In vivo* infection experiments performed by T.M.
1055 and A.M. J.R. provided bacterial strains and guided the infection studies. The
1056 manuscript was written by T.M. D.S.K. and A.M with contributions and comments
1057 from all authors.

1058

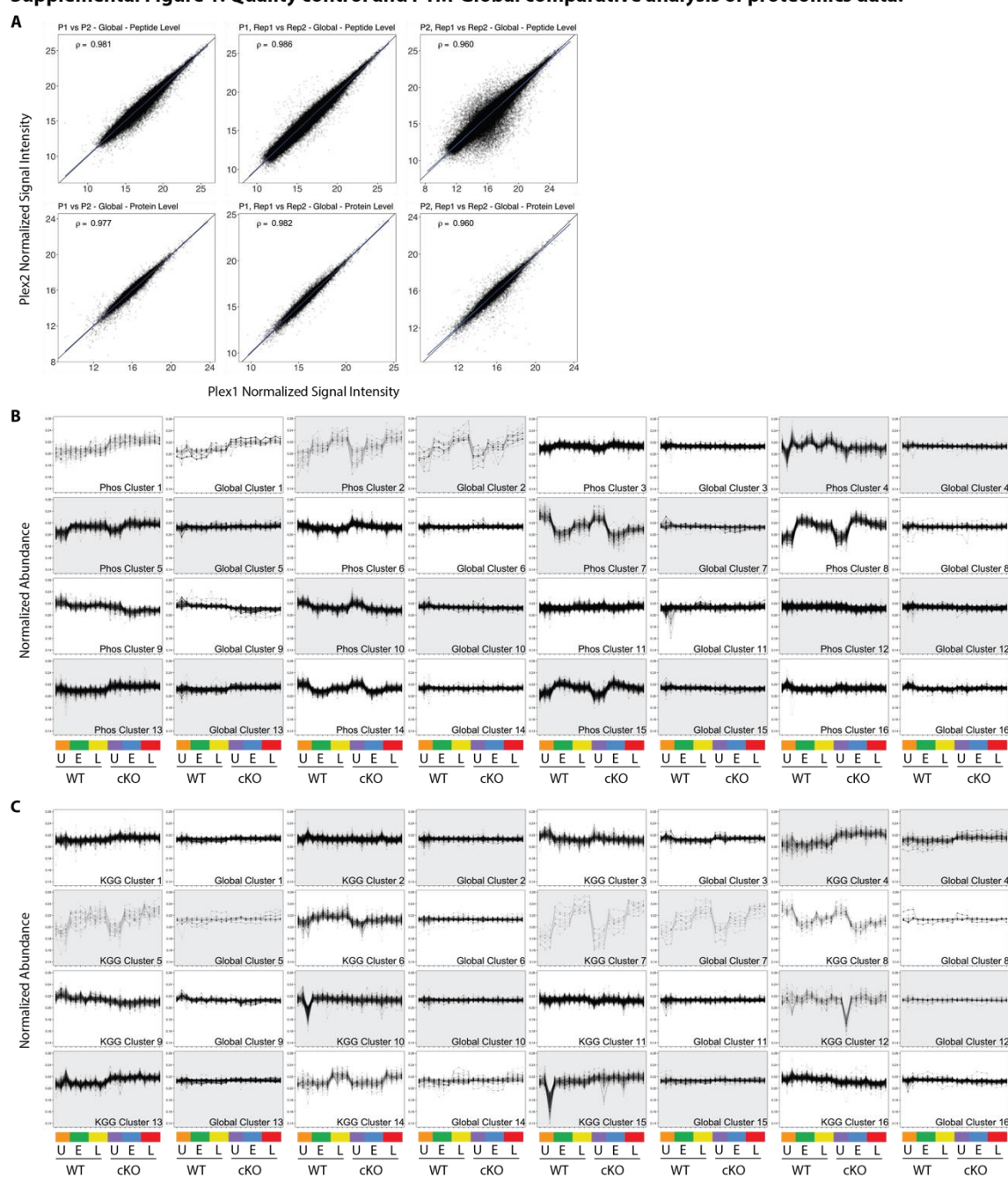
1059 **Competing interests**

1060 T.M., T.H., P.C., C.C., J.L., A.K.K., M.R., D.S.K. and A.M. are current
1061 employees of Genentech Inc. and shareholders in Roche. I.D. is a current employee
1062 of Fraunhofer Institutes, CEO and co-founder of Vivlion GmbH, and co-founder of
1063 Caraway Therapeutics. R.C.K. and B.K.E. are current employees of IQ Proteomics
1064 LLC. E.V. is a current employee at Galapagos.

1065

Supplemental Figures and Tables

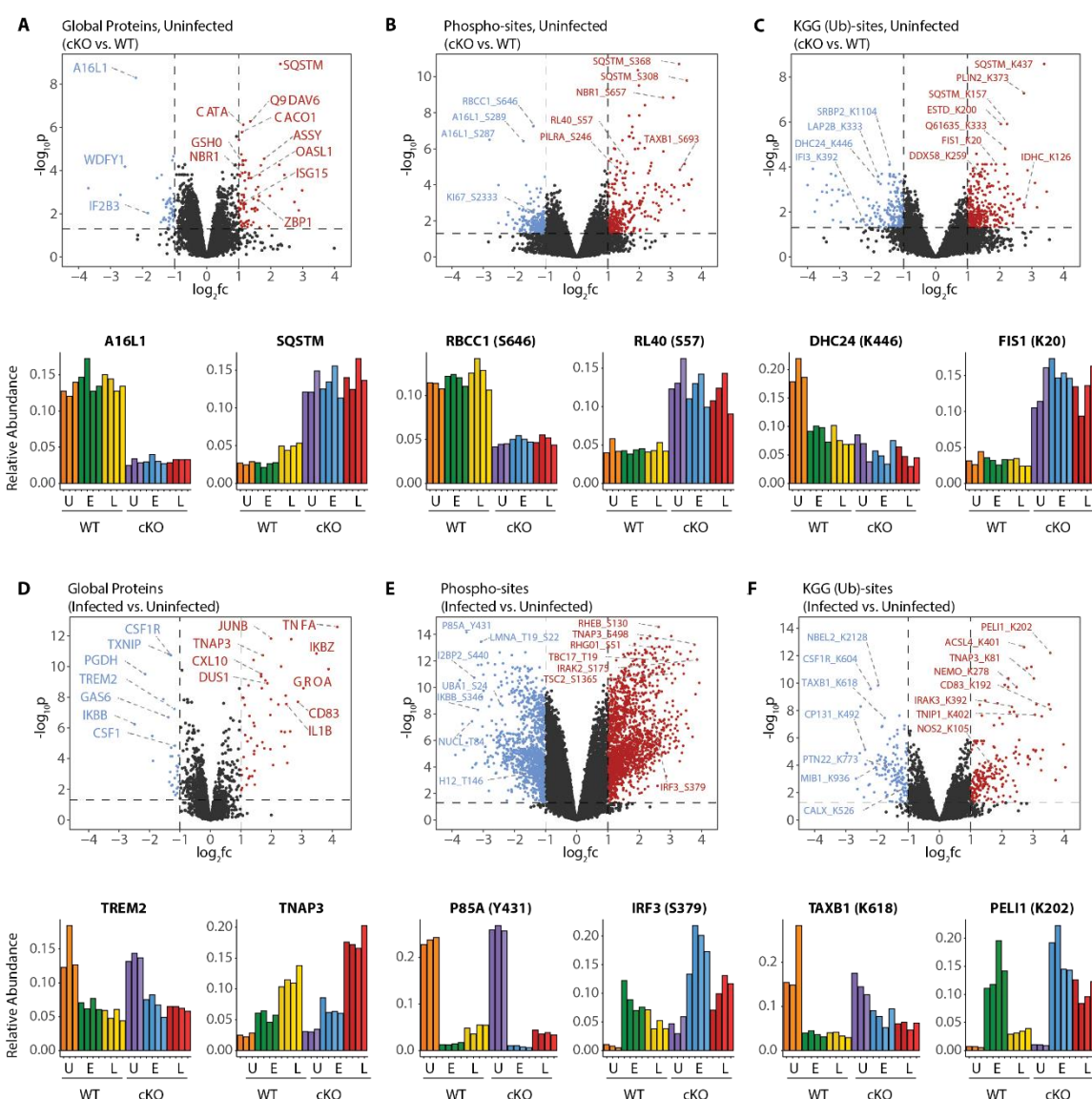
Supplemental Figure 1. Quality control and PTM-Global comparative analysis of proteomics data.



(A) Scatterplots showing normalized signal intensity from the Global Proteome analysis. Peptide (upper row) and protein (lower row) level data stemming from MSstats modeling are displayed. Plots in the first column compare Plex 1 versus Plex 2, where data from intra-plex duplicates was aggregated during modeling. Plots in the middle and right columns compare intra-plex duplicate samples within Plex1 (middle) or Plex2 (right). Pearson correlations are shown for each contrast. (B and C) Line plots showing all 16 K-means clusters corresponding to the Phospho-Global (B) and KGG (Ub)-Global (C) heatmaps displayed in Figure 2. The background shading for each pair of line plots is toggled to highlight pairing between Phos/KGG and Global protein clusters.

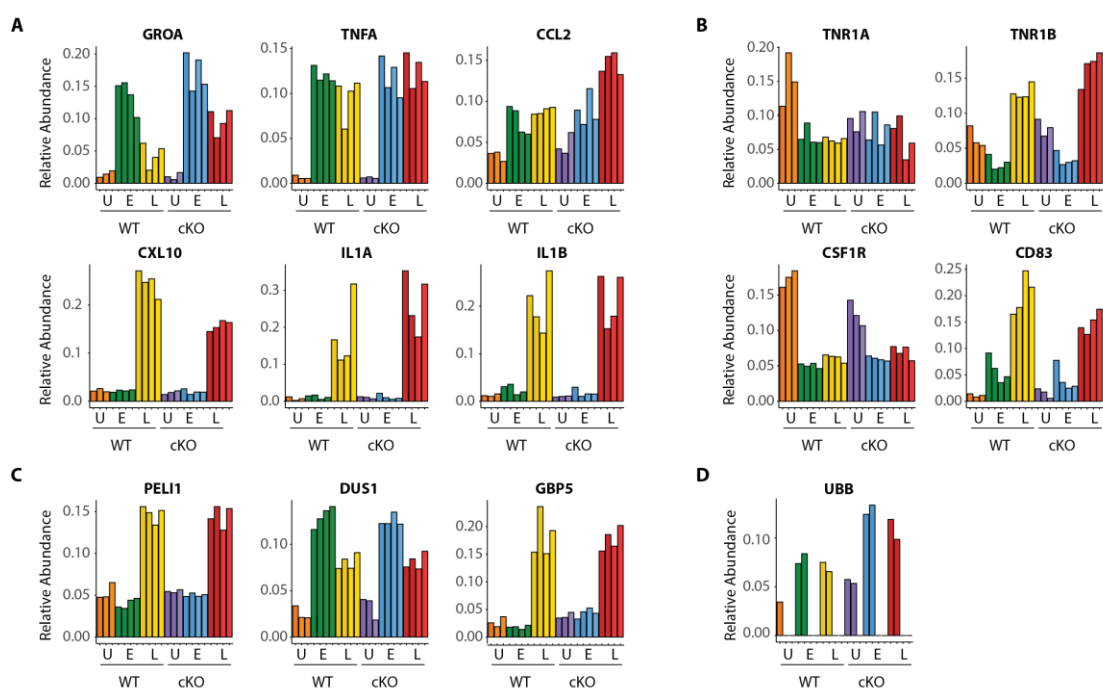
1066

Supplemental Figure 2. A global overview of changes identified between the genotypes and upon infection.



(A-C) Volcano plots showing differential expression of Global Proteins (A), Phospho-sites (B) and KGG (Ub)-sites (C) between uninfected cKO vs. WT BMDMs. Volcano plots display \log_2 fold changes and $-\log_{10}$ transformed p-values for the host proteome. Bar graphs at the bottom of each panel represent top hits with positive and negative \log_2 fold changes. Uninfected (U) samples are shown with orange (WT) and purple (cKO), early infection (E) in green (WT) and blue (cKO) and late infection in yellow (WT) and red (cKO), respectively. Protein names are shown as UniProt identifiers with modification sites indicated by the modified amino acid (S/T/Y/K) and residue number (e.g. RL40_S57). Features enriched in cKO and WT BMDMs are highlighted in red and blue, respectively. (D-F) Volcano plots displaying differentially expressed Global Proteins (D), Phospho-sites (E) and KGG (Ub)-sites (F) between infected and uninfected BMDMs. Infected refers to the aggregate condition in which early (E) and late (L) infected samples for WT and cKO are each weighted as 0.25 relative to 0.5 each for the WT and cKO uninfected samples. Features enriched in infected and uninfected BMDMs are highlighted in red and blue, respectively. As above, bar graphs below each panel show example hits. The relative abundance of TMT reporter ions sums up to 2.0 for features quantified in both Plex1 and Plex2.

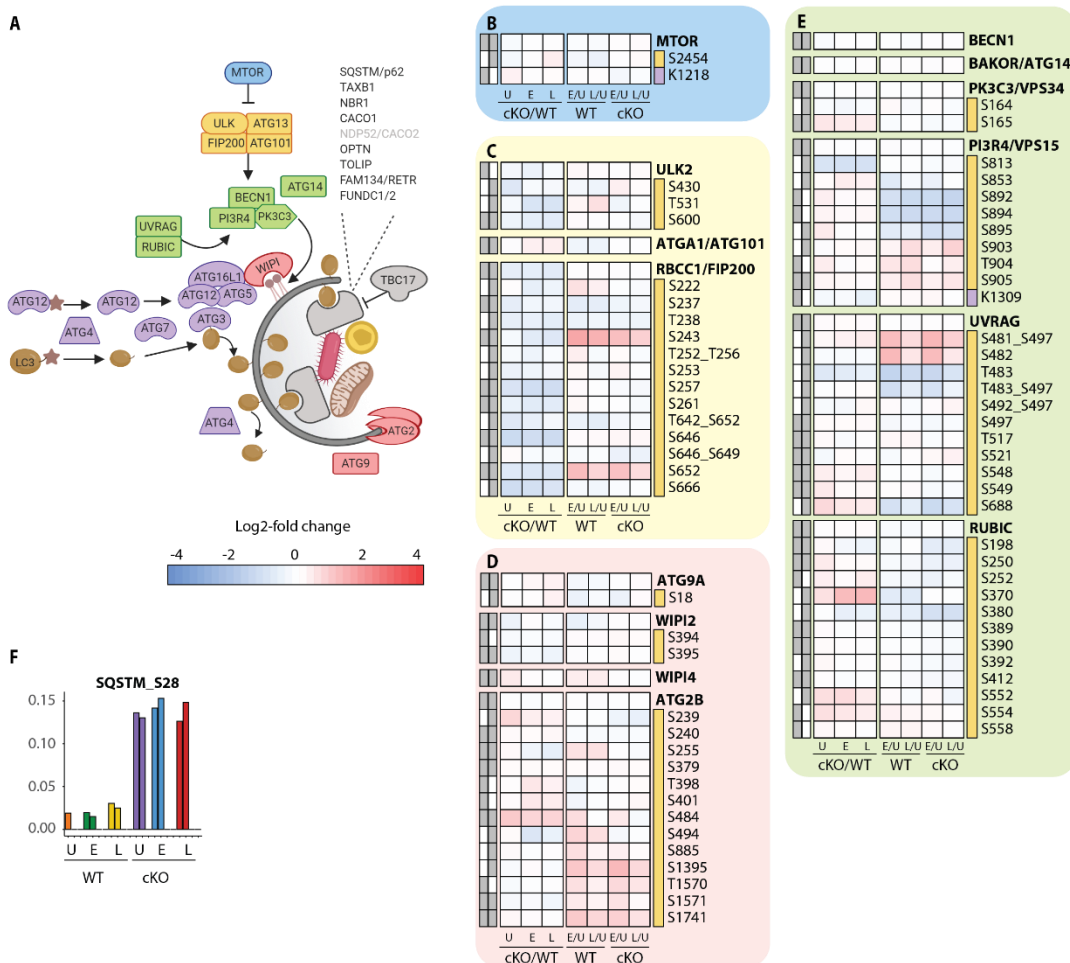
Supplemental Figure 3. Dynamic macrophage response to infection.



(A-D) Bar graphs showing quantitative changes for representative pro-inflammatory cytokines and chemokines (A), cell surface receptors (B), components of innate immune signaling (C) and linear ubiquitin chains as represented by UBB (D).

1068

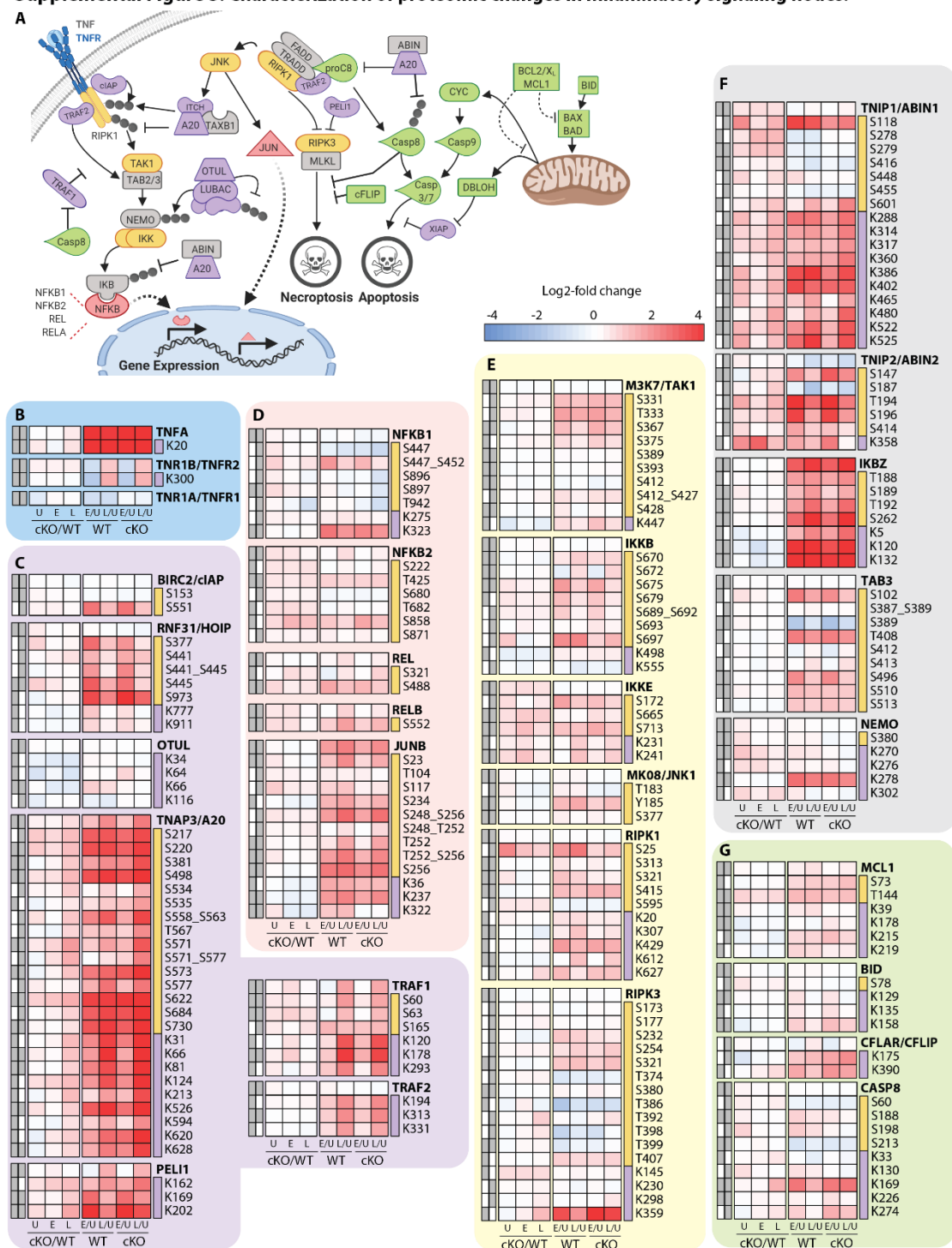
Supplemental Figure 4. Extended analysis of proteomic changes in the autophagy pathway.



(A) Schematic representation of macro-autophagy & selective autophagy machinery as shown in Figure 3C. (B-E) Heatmap representations of mTOR (B), ULK complex (C), membrane recruitment and closure (D), and PIK3C3/Vps34 complexes (E) are shown. The background shading for each panel corresponds to the functional color coding of proteins in the pathway schematic shown in (A). (F) Bar graph showing phosphorylation on autophagy receptor p62 (SQSTM_S28).

1069

Supplemental Figure 5. Characterization of proteomic changes in inflammatory signaling nodes.

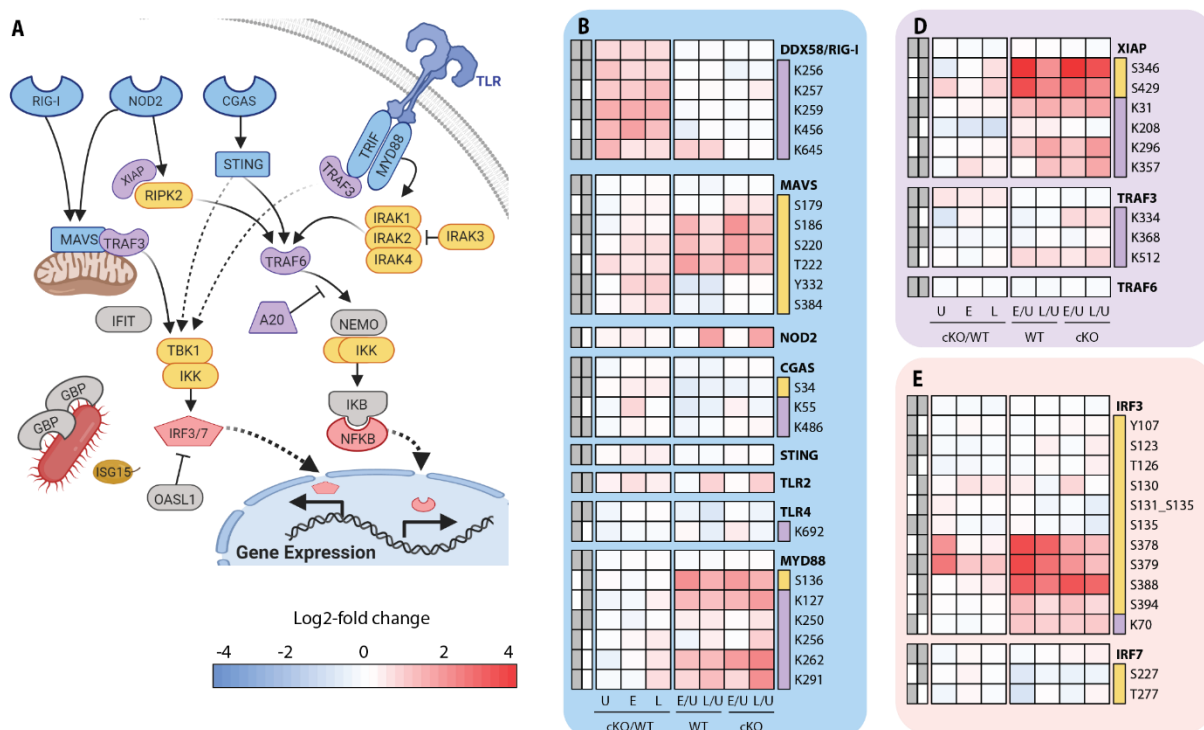


(A) Schematic representation of key components in the inflammatory signaling and programmed cell death pathways analyzed in this study. (B-G) Heatmap representations of TNF and its receptors (B), E3 ubiquitin ligase and deubiquitinase enzymes (C) and transcription factors (C), kinases (E), signaling adaptors (F), and apoptosis regulatory proteins (G). The background shading for each panel corresponds to the functional color coding of proteins in the pathway schematic shown in (A).

1070

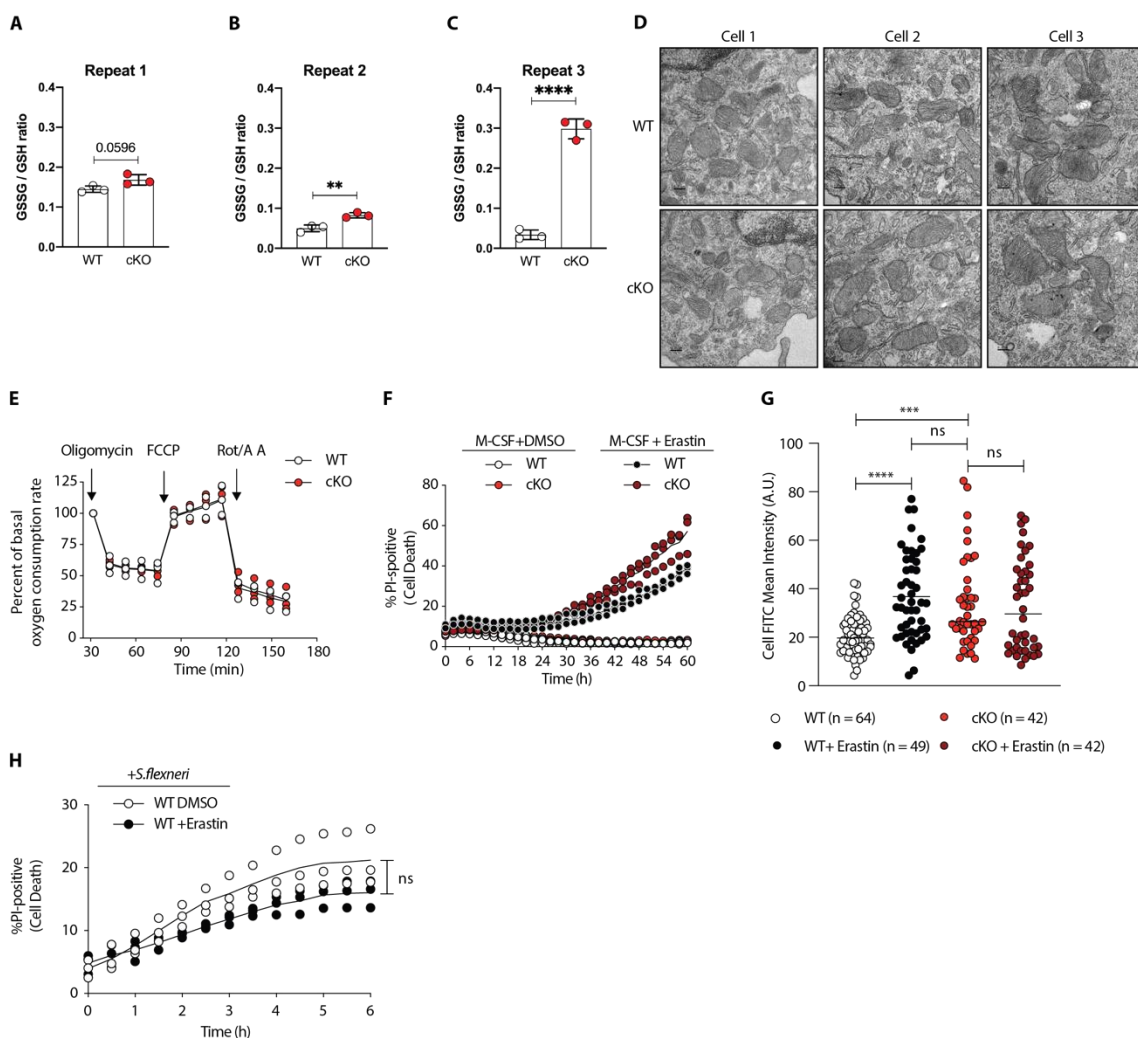
1071

Supplemental Figure 6. Analysis of proteomic changes in innate sensing and the interferon response.



(A) Schematic representation of innate sensors and inflammatory signaling components analyzed in this study. (B-F) Heatmap representations of microbe-associated molecular pattern receptors and adaptors (B), kinases (C), E3 ubiquitin ligases (D), transcription factors (E) and interferon response genes (F) are shown. The background shading for each panel corresponds to the functional color coding of proteins in the pathway schematic shown in (A).

Supplemental Figure 7. Elevated oxidative stress in ATG16L1-deficient macrophages.



(A-C) Graphs show three independent experiments quantifying the GSSG/GSH ratio in BMDMs from three different preparations. Unpaired t test ** P = 0.0057, **** P < 0.0001. (D) Representative electron microscopy (EM) micrographs of WT and cKO BMDMs at magnification 8000x (scale bar = 0.2 μ m). (E) Seahorse assay showing oxygen consumption rate of WT and cKO BMDMs. Graph shows the percent of basal respiration following treatment with 1.5 μ M oligomycin, 1 μ M FCCP and 0.5 μ M Rotenone/Antimycin A from three independent experiments using three different BMDM preparations (n = 3). (F) Percentage of PI-positive WT and cKO BMDMs during time-course incubation with DMSO or 4 μ g/ml Erastin. A representative graph shows individual values from three wells from one experiment (n = 3). (G) Quantification of CellRox green probe mean intensity in WT and cKO BMDMs in the absence or presence of Erastin 4 μ g/ml for 24h. Graph shows single cell data from one experiment (n = 3). Ordinary one-way ANOVA Tukey's multiple comparison test **** P < 0.0001 and *** P = 0.0003. A part of the data is also used in Figure 4E. (H) Percentage of PI-positive WT BMDMs during time-course infection with *S.flexneri* M90T in the presence of DMSO or Erastin 4 μ g/ml. Graph represents individual values from three independent experiments using three different BMDM preparations. ns, non-significant.

1074 **Supplemental Table 1. Composition PTM-Site and Global Protein clusters**
1075 **displayed in Figure 1F, 1G and S1b, S1C.**

1076

1077 **Supplemental Table 2. Curated list of PTMs described in Figure 3 and S3 with**
1078 **associated references.**

1079

1080 **Supplemental Table 3. Curated list of PTMs described in Figure 4 and S4 with**
1081 **associated references.**

1082

1083 **Supplemental Table 4. Gene Set Enrichment Analysis (GSEA) performed to**
1084 **identify cellular processes overrepresented in ATG16L1 deficient BMDMs in**
1085 **Figure 5A.**

1086

1087 **Supplemental Table 5. Protein references and gene names associated with**
1088 **mitochondrial and peroxisomal categories in Figure S5A-C.**

1089

1090 **Supplemental Table 6. MSstatsTMT normalized quantification report for Global**
1091 **Proteins data.**

1092

1093 **Supplemental Table 7. MSstatsTMT statistical testing results for Global**
1094 **Proteins data.**

1095

1096 **Supplemental Table 8. MSstatsTMT normalized quantification report for**
1097 **Phosphorylation Site data.**

1098

1099 **Supplemental Table 9. MSstatsTMT normalized quantification report for KGG**
1100 **(Ub)-sites data.**